Article

Jet stream controls on European climate and agriculture since 1300 CE

https://doi.org/10.1038/s41586-024-07985-x

Received: 22 March 2024

Accepted: 21 August 2024

Published online: 25 September 2024

Open access

Check for updates

Guobao Xu[1,2,3], Ellie Broadman[2], Isabel Dorado-Liñán[4], Lara Klippel[5], Matthew Meko[2], Ulf Büntgen[6,7,8,9], Tom De Mil[2,10], Jan Esper[7,11], Björn Gunnarson[12], Claudia Hartl[13,14], Paul J. Krusic[6,15], Hans W. Linderholm[16], Fredrik C. Ljungqvist[15,17,18], Francis Ludlow[19], Momchil Panayotov[20], Andrea Seim[21,22], Rob Wilson[23], Diana Zamora-Reyes[2] & Valerie Trouet[2,24] ✉

The jet stream is an important dynamic driver of climate variability in the Northern Hemisphere mid-latitudes[1–3]. Modern variability in the position of summer jet stream latitude in the North Atlantic–European sector (EU JSL) promotes dipole patterns in air pressure, temperature, precipitation and drought between northwestern and southeastern Europe. EU JSL variability and its impacts on regional climatic extremes and societal events are poorly understood, particularly before anthropogenic warming. Based on three temperature-sensitive European tree-ring records, we develop a reconstruction of interannual summer EU JSL variability over the period 1300–2004 CE (R^2 = 38.5%) and compare it to independent historical documented climatic and societal records, such as grape harvest, grain prices, plagues and human mortality. Here we show contrasting summer climate extremes associated with EU JSL variability back to 1300 CE as well as biophysical, economic and human demographic impacts, including wildfires and epidemics. In light of projections for altered jet stream behaviour and intensified climate extremes, our findings underscore the importance of considering EU JSL variability when evaluating amplified future climate risk.

Under anthropogenic climate change, the Northern Hemisphere subpolar jet stream is projected by most models to weakly shift poleward and to show enhanced sinuosity[1,2]. A wavier jet stream can result in more persistent and extreme jet stream anomalies that strongly affect mid-latitude weather patterns[3]. An amplified meridional configuration of the jet stream and the resulting jet stream latitudinal extremes can cause more intense and frequent extreme weather events, including increased persistence of summer heatwaves, droughts, floods and wildfires[1,4], that can exacerbate and compound anthropogenically driven climate extremes[5,6].

Intensified upper-level wind speed and vertical wind shear under climate change may also contribute to more severe climate extremes[7] and quasi-resonance in the jet stream system can result in hemispheric-scale synchronization of climate extremes[6,8]. With this multitude of drivers, many types of climate extreme are projected to increase in frequency, duration and intensity under anthropogenic warming and their interactions are projected to lead to compounding hazards and risks[6,9,10].

During recent decades, the number of climate extremes affecting the Northern Hemisphere mid-latitudes has increased[5,9,10] and the associated societal impacts have intensified in high-risk regions[11,12]. Crop production, for instance, can be disrupted by extreme weather events such as droughts, floods and extreme heat[12–14]. The growth and yield of maize, for example, the main crop cultivated in numerous regions worldwide, are strongly affected by water and heat stress[15]. Year-to-year yield variability can destabilize crop production and pose a serious challenge to food security[13], even when it is superimposed on an increasing trend in the yield of the main cereal crops that is driven by improvements in crop production technology and management[14], as well as by efforts to breed better climate-adapted plant species and varieties[16]. Moreover, the synchronization of climate extremes in key crop production regions across the globe can threaten food security on a global scale[17].

The role of jet stream variability and configuration in triggering concurrent climate extremes that can synchronize harvest failures and

[1]Shaanxi Key Laboratory of Earth Surface System and Environmental Carrying Capacity, College of Urban and Environmental Sciences, Northwest University, Xi'an, China. [2]Laboratory of Tree-Ring Research, University of Arizona, Tucson, AZ, USA. [3]State Key Laboratory of Cryospheric Sciences, Northwest Institute of Eco-Environment and Resources, Chinese Academy of Sciences, Lanzhou, China. [4]Departamento de Sistemas y Recursos Naturales, Universidad Politécnica de Madrid, Madrid, Spain. [5]Geschäftsbereich Klima und Umwelt, Deutscher Wetterdienst, Offenbach, Germany. [6]Department of Geography, University of Cambridge, Cambridge, UK. [7]Global Change Research Institute, Czech Academy of Sciences (CzechGlobe), Brno, Czech Republic. [8]Swiss Federal Institute for Forest, Snow and Landscape Research WSL, Birmensdorf, Switzerland. [9]Department of Geography, Faculty of Science, Masaryk University, Brno, Czech Republic. [10]Forest Is Life, TERRA Teaching and Research Centre, Gembloux Agro Bio-Tech, University of Liège, Gembloux, Belgium. [11]Department of Geography, Johannes Gutenberg University, Mainz, Germany. [12]Stockholm Tree Ring Laboratory, Department of Physical Geography, Stockholm University, Stockholm, Sweden. [13]Nature Rings – Environmental Research and Education, Mainz, Germany. [14]Panel on Planetary Thinking, Justus-Liebig-University, Gießen, Germany. [15]Department of History, Stockholm University, Stockholm, Sweden. [16]Regional Climate Group, Department of Earth Sciences, University of Gothenburg, Gothenburg, Sweden. [17]Bolin Centre for Climate Research, Stockholm University, Stockholm, Sweden. [18]Swedish Collegium for Advanced Study, Linneanum, Uppsala, Sweden. [19]Trinity Centre for Environmental Humanities and Department of History, Trinity College Dublin, Dublin, Ireland. [20]Dendrology Department, University of Forestry, Sofia, Bulgaria. [21]Chair of Forest Growth and Dendroecology, Institute of Forest Sciences, University of Freiburg, Freiburg, Germany. [22]Department of Botany, University of Innsbruck, Innsbruck, Austria. [23]School of Earth and Environmental Sciences, University of St Andrews, Fife, UK. [24]Belgian Climate Centre, Uccle, Belgium. ✉e-mail: trouet@arizona.edu

food security risks has been established at the hemispheric scale[17]. Yet, jet stream variability and waviness are also reflected in regional-scale climate patterns and extremes[18,19]. Whereas regional-scale jet stream variability has been shown to affect ecosystem functioning and disturbances[4,20,21], its societal impacts are largely undocumented.

In Europe, jet stream latitude (JSL) varies on daily[22], seasonal[19] and annual to-multi-decadal time scales[23] and is a primary dynamic driver of summer weather and climate extremes. European summer weather extremes are dynamically associated with the strength and persistence of cyclonic or anticyclonic (blocking) weather regimes[24,25], which in turn are related to the configuration of the mid-latitude jet stream over the North Atlantic–European (EU) domain[18,20]. However, given short observational records and model biases, further insight into summer jet stream dynamics to understand how climate warming might affect the JSL, including its latitudinal displacements, is needed.

Here we present a tree-ring-based reconstruction of variability in summer JSL in the North Atlantic–Europe region (EU JSL) over the period 1300–2004 CE and use independent documentary data to investigate societal impacts of past EU JSL extremes. Annually resolved, tree-ring-based reconstructions of storm tracks[26] and jet stream variability[4,23] have illustrated the power of this proxy to investigate past climate dynamics. The 700+-year timespan of our study provides an opportunity to quantify changes in the frequency and intensity of climate extremes in Europe and their dynamic drivers. With its robust historical records of past conditions[27–29], the European continent provides an optimal setting to investigate the regionally explicit influence of pre-industrial JSL variability on climate extremes and their associated societal impacts.

Modern summer EU JSL impacts

Summer weather patterns in Europe are dynamically driven by JSL variability expressed by two main modes that collectively explain more than half of the JSL variance[20]. The second mode, represented by the second principal component (PC) of the JSL (Methods and Extended Data Fig. 1), captures late summer (July–August) JSL variability over the European continent and is closely related to climate extremes experienced here (Fig. 1).

Anomalously northern EU JSL positions coincide with a trough over the northeastern Atlantic and anticyclonic conditions over southern Europe, propelling the JSL northward (Fig. 1a, Extended Data Fig. 2a,b and Extended Data Table 1). These excursions lead to cool and wet conditions over the British Isles (BRIT), whereas the northeastern Mediterranean (NEMED) experiences warm and dry summers, with temperature anomalies of up to 1 °C (Fig. 1c,e,g and Extended Data Fig. 2c–h). Reversed conditions occur when the summer EU JSL is positioned southwards (Fig. 1b), with an increased frequency of northerly blocking and anticyclonic conditions leading to warm and dry weather over BRIT, concomitant with increased cyclonic tendencies over southern Europe that promote relatively cool and wet conditions over NEMED (Fig. 1d,f,h).

Northern and southern summer EU JSL excursions thus induce a dipole between BRIT and NEMED summer weather that is reflected not only in a variety of climate variables (Fig. 1) but also in vegetation productivity. From 1950 to 2005 CE, extreme northern and southern EU JSL positions induced anomalies of up to 30% in modelled gross primary productivity and 50% in radial tree growth of European drought-sensitive beech[20].

Summer EU JSL variability also affects agricultural yields of major cereal crops, such as maize and wheat, particularly in NEMED (Fig. 2 and Extended Data Fig. 3). NEMED maize and wheat yields (1981–2016 CE) are anomalously low during dry and hot northern EU JSL summers (Fig. 2a,c and Extended Data Fig. 3), whereas southern EU JSL anomalies result in cool and wet NEMED summers and above-average maize and wheat yields (Fig. 2b,d and Extended Data Fig. 3). The NEMED results also highlight that wheat is more tolerant to climate extremes than maize[30]. NEMED wheat yield generally decreases during northern EU JSL summers and increases during southern EU JSL summers, but the anomalies are weaker and less homogeneous than for maize.

The impact of summer EU JSL variability on crop yield is weaker in BRIT compared with NEMED (Fig. 2 and Extended Data Fig. 3) but is generally of the same sign and crop yield thus does not reflect the EU-JSL-driven climate dipole between both regions. Similar to NEMED yield, BRIT wheat yield is generally lower than average during northern and higher than average during southern EU JSL excursions (Fig. 2c,d and Extended Data Fig. 3).

EU JSL reconstruction (1300–2004 CE)

We combined three well-replicated, temperature-sensitive tree-ring records to reconstruct summer EU JSL variability over the period 1300–2004 CE (Fig. 3a,b and Methods). We developed a new tree-ring maximum latewood density (MXD) record for NEMED and combined it with the existing records from BRIT[31] and the Alps (ALP)[32] (Methods and Extended Data Table 2). Each of the tree-ring chronologies extends back to at least 1300 CE, encodes a robust temperature signal strength and is significantly positively correlated with regional instrumental July–August temperature (r = 0.49 to 0.61; $P \leq 0.01$; Extended Data Table 2). These correlations remain significantly positive after high- and low-pass filtering (Methods), showing consistent sensitivity to temperature across frequency domains (Extended Data Table 2). All chronologies are significantly correlated with the instrumental summer EU JSL target, with a negative correlation for the BRIT chronology (r = −0.27, $P \leq 0.05$) and positive correlations for the ALP and NEMED chronologies (r = 0.36 and 0.47 respectively, $P \leq 0.05$). The sign of these correlations reflects the EU-JSL-driven summer climate dipole over Europe: during northern (positive) EU JSL summers, climate conditions in BRIT are cooler and wetter than average (Fig. 1 and Extended Data Fig. 2), resulting in low density and negative tree-ring anomalies. In NEMED and ALP, the conditions are warmer and drier than average during northern EU JSL summers, resulting in high-density values and positive tree-ring anomalies. The reverse pattern occurs during southern (negative) EU JSL summers. Our reconstruction explains 38.5% (R^2_{adj} = 38.5%, r = 0.65; $P \leq 0.001$; Extended Data Table 3a) of summer EU JSL variability over the observational period (1948–2004 CE; Fig. 3a) without trends in the regression model residuals (Extended Data Fig. 4a–d), indicating preservation of high- and low-frequency variability (Extended Data Fig. 4e,f). The calibration and verification results show that summer EU JSL can be skillfully reconstructed back to 1300 CE, with 34–41% of the variance explained and positive reduction of error (RE) and coefficient of efficiency (CE) values (Extended Data Table 3b).

To optimize explained variance and sample replication, we combined MXD chronologies from opposite ends of the summer EU JSL dipole, with the trade-off that this approach constrained our ability to retain low-frequency variability (Methods). As such, our EU JSL reconstruction is dominated by inter-annual to multi-decadal-scale variability (Fig. 3b) and well-studied centennial-scale periods in European climate, such as the colder phases of the Little Ice Age[33], do not emerge. Nevertheless, a multi-decadal southern EU JSL anomaly from 1810 to 1839 CE overlaps with the cold early-nineteenth-century end phase of the Little Ice Age. The years 1813–1816 CE in particular, the southernmost EU JSL years on record, coincide with the eruptions of the tropical Mayon (1814 CE) and Tambora (1815 CE) volcanoes[34], suggesting a potential link between EU JSL position and volcanic activity that could have exacerbated the cold summer temperatures in NEMED.

Recent summer EU JSL values fall within the range of preceding centuries, except for the summer of 2010, which exhibits the northernmost EU JSL position in the instrumental record but is not captured by our reconstruction (1300–2004 CE). Other recent northern EU JSL

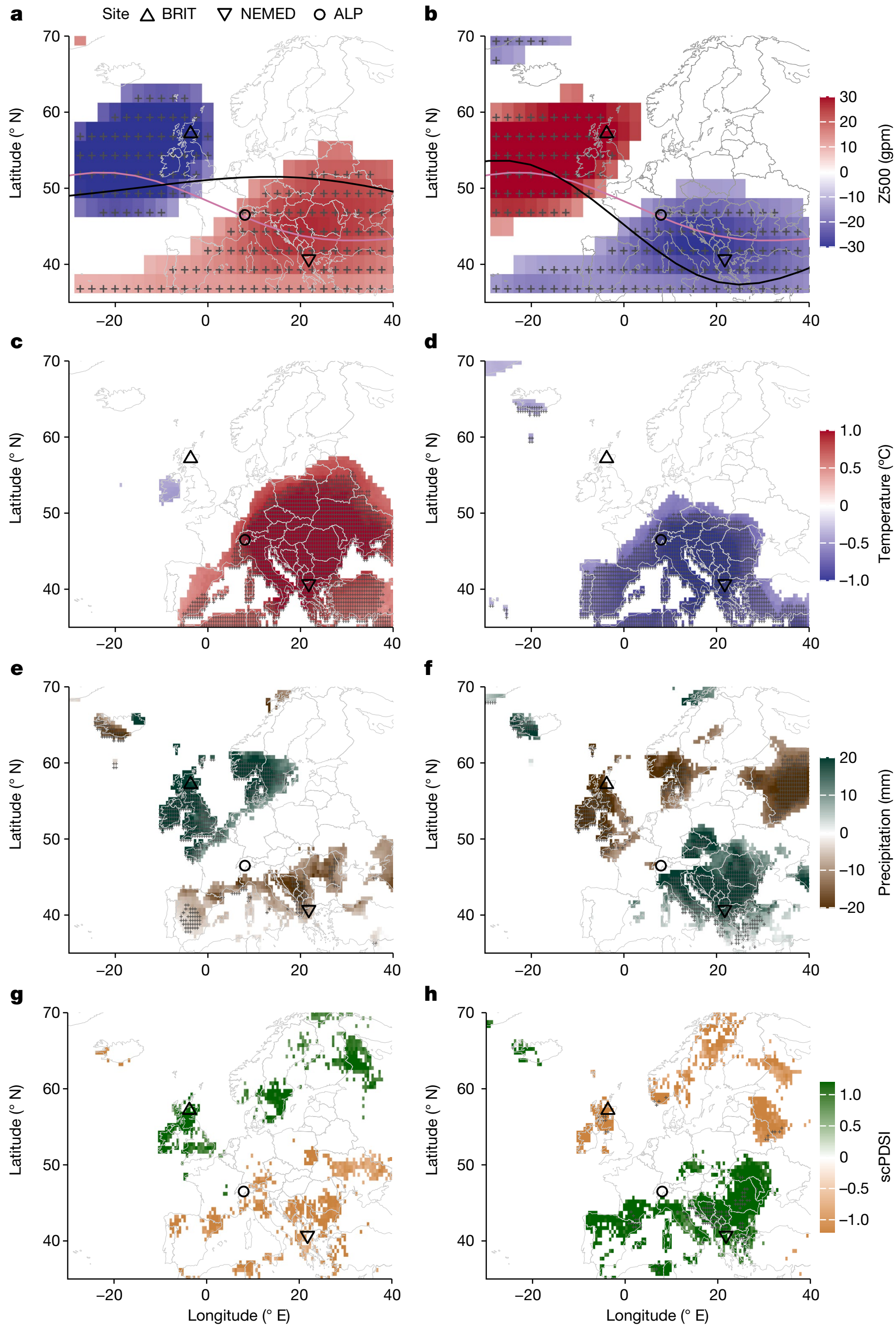

Fig. 1 | Influence of summer (July–August) EU JSL on European climate (1948–2018 CE). **a**–**h**, Composite maps for years (Extended Data Table 1) with extremely positive (D80, north, $n = 15$ years) and negative (D20, south, $n = 15$ years) summer EU JSL values show associated anomalies in NCEP/NCAR July–August 500 hPa geopotential height (Z500) (**a**,**b**), CRU ts4.05 July–August temperature (**c**,**d**), July–August precipitation (**e**,**f**) and July–August scPDSI (**g**,**h**). In **a**–**h**, coloured composite maps are shown only where $P \leq 0.1$, and areas with statistically significant values after controlling for the false discovery rate ($\alpha_{FDR} \leq 0.1$) are cross-hatched. In **a** and **b**, the mean July–August jet position for 1948–2018 CE (pink line) and for the 15 extreme positive years (northward EU JSL position, **a**) and extreme negative years (southward EU JSL position, **b**) (black line) are shown. Locations of the tree-ring chronologies used in the EU JSL reconstruction are indicated by the symbols at the centre of the site network of each chronology. Composite maps were created in R. gpm, geopotential metre.

anomalies, such as 2018, are similar in magnitude to historical northern anomalies (for example, 1387 CE and 1782 CE). Recent southern EU JSL anomalies (for example, 1955 CE and 2002 CE) are exceeded by southern positions in the early fourteenth and nineteenth centuries (Fig. 3b). Overall, the number of EU JSL extremes has increased in the nineteenth and twentieth centuries, with 40% more northern and southern EU JSL extremes compared with previous centuries (Extended Data Table 4).

Correlation maps between our summer EU JSL reconstruction and independent, gridded field reconstructions of summer 500 hPa geopotential height (Z500; 1659–2000 CE) (ref. 35), temperature (1766–2000 CE) (ref. 36), precipitation (1766–2000 CE) (ref. 36) and self-calibrating Palmer Drought Severity Index (scPDSI, 1300–2004 CE) (ref. 37) consistently show contrasting conditions over northwestern versus southeastern Europe that are consistent with twentieth-century patterns (Extended Data Fig. 5). These patterns are, therefore, robust through time, except for the nineteenth century, when volcanic activity dominated European temperature patterns and weakened the EU-JSL-driven dipole.

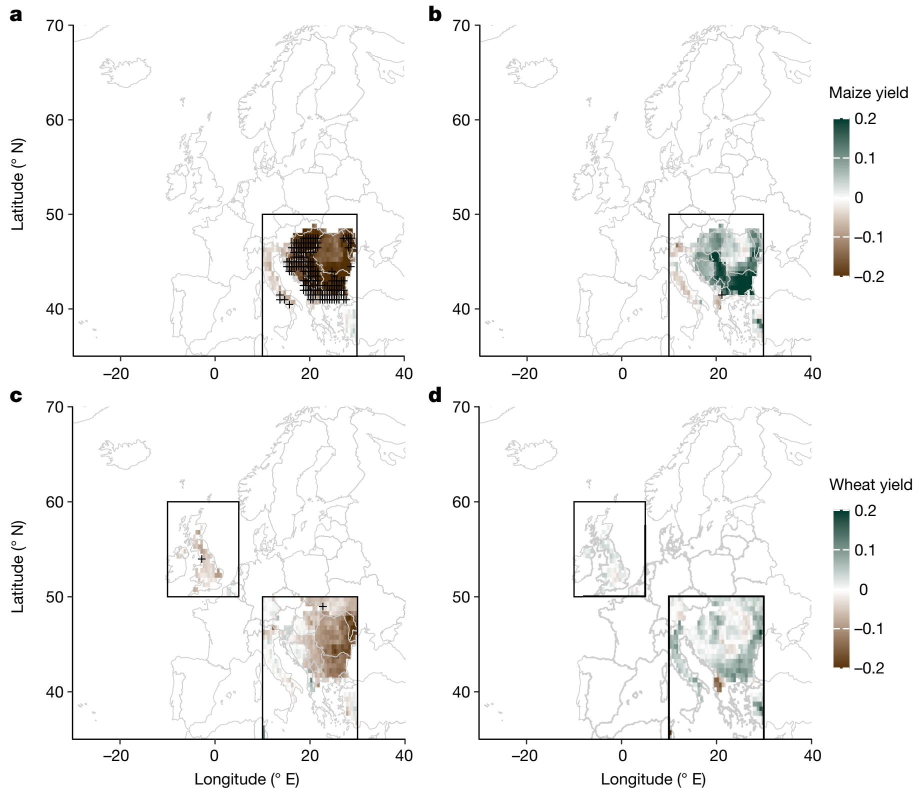

Fig. 2 | Influence of EU JSL extremes on crop yield (1981–2016 CE). **a**–**d**, Composite analysis maps of gridded maize (**a**,**b**) and wheat (**c**,**d**) yield for extremely northern (**a**,**c**; D80, $n = 8$ years) and southern (**b**,**d**; D20, $n = 8$ years) EU JSL positions over the period 1981–2016 CE. Maize yield composites were calculated for the NEMED region (no substantial maize data are available for the BRIT region) and wheat yield composites were calculated for the BRIT and NEMED regions. Coloured composite maps are shown only where $P \leq 0.1$ and areas with statistically significant results after controlling for the false discovery rate ($\alpha_{FDR} \leq 0.1$) are cross-hatched. Black boxes show the locations of BRIT and NEMED regions. Crop yield data were derived from the Global Dataset of Historical Yield gridded dataset and were detrended using a 20-year smoothing spline (Methods).

Historical summer EU JSL and impacts

The climate dipole between BRIT and NEMED also emerges in independently reconstructed historical climate extremes when compositing past EU JSL extreme summers (Fig. 3c–j). The pattern is further reflected in composites of extreme climate years in BRIT and NEMED derived from independent historical documentary datasets (Fig. 4, Methods and Extended Data Table 5). During past centuries, hot and dry extremes in NEMED have occurred predominantly during northern EU JSL anomalies and wet and cold extremes in NEMED have occurred predominantly during southern EU JSL anomalies (Fig. 4). The opposite pattern arises in BRIT, where hot and dry BRIT summers are characterized by southern EU JSL anomalies and wet and cold BRIT summers are characterized by northern EU JSL anomalies (Fig. 4). These EU JSL anomalies are least pronounced for cold BRIT summers (Fig. 4b), corroborating the comparatively weak BRIT temperature anomalies of the EU JSL composite analyses (Figs. 1c,d and 3e,f).

Apart from historical temperature and precipitation extremes, significant EU JSL anomalies also occurred during years experiencing pronounced natural hazards (Figs. 4d and 5c). Historically documented summer floods in NEMED have generally occurred when southern EU JSL anomalies drive wet and cool conditions (Fig. 4d), whereas historical wildfire years (1450–1940 CE; Methods) occurred mostly during northern EU JSL anomalies that drive hot and dry NEMED conditions (Fig. 5c).

Years of pronounced agricultural and biophysical extremes were also frequently characterized by significant EU JSL anomalies (Fig. 5). Regional impacts of past EU JSL variability were more pronounced for historical NEMED grape harvests, particularly during poor grape harvest years, compared with grain prices (Fig. 5a,b). This may be because, compared with yield, grain price is a more indirect proxy of agricultural productivity that is influenced by many more factors other than climate[38,39]. Nevertheless, grain price results are in line with grain yield results for the modern period (Fig. 2): BRIT and NEMED grain prices show similar EU JSL response patterns, despite contrasting climatic conditions between the two regions (Fig. 5a). NEMED wheat prices were low, indicating above-average yields, during cool southern EU JSL summers (Fig. 5a). Also BRIT grain prices were relatively low in years when the EU JSL was in a southern position, but BRIT summers were relatively dry. By contrast, BRIT grain prices were typically slightly higher following the cold and wet conditions of northern EU JSL summers.

Historical grape yield datasets are not available from BRIT, but in NEMED, cool southern EU JSL summers had a distinct negative effect on grape harvest, including harvest delays, low yields and poor wine quality (Fig. 5b and Extended Data Fig. 6a). This historical influence of EU JSL position on NEMED grape harvests is corroborated by modern grape yields, which show anomalously low yields following southern EU JSL summers (Extended Data Fig. 6b). By contrast, historical NEMED grape harvest typically occurred early in the hot and dry summers of northern EU JSL anomalies, resulting in good grape harvests, early grape ripening and harvest dates and wine quality (Extended Data Fig. 6a).

The EU-JSL-induced dipole between NEMED and BRIT is also imprinted in historical records of biophysical and demographic extremes, including wildfires, epidemics and human mortality (Fig. 5c). In NEMED, plague years were predominantly associated with the cold and wet summers of southern EU JSL anomalies. These patterns are reversed for BRIT, where increases in epidemics and human mortality followed cold and wet northern EU JSL summers.

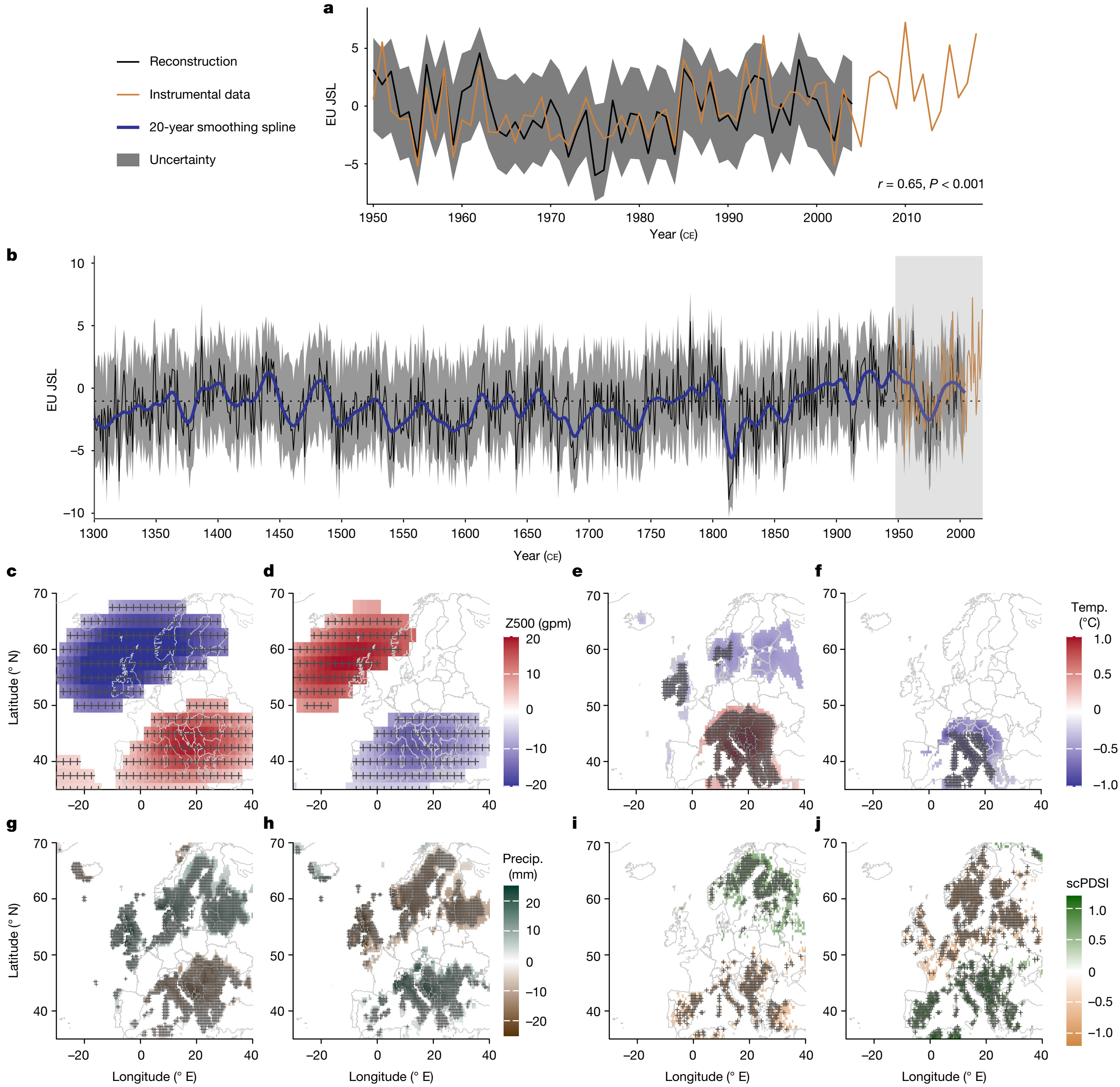

Fig. 3 | Reconstructed summer EU JSL from 1300 to 2004 CE with composited extreme summer EU JSL years for climate variables in Europe. **a**, Comparison between reconstructed summer EU JSL and instrumental summer EU JSL (1948–2004 CE). **b**, Reconstructed summer EU JSL from 1300 to 2004 CE with uncertainty (Methods; grey shading). The blue line shows the low-frequency variability of the reconstruction (20-year cubic smoothing spline) and the dotted line shows the mean. Grey vertical shading indicates the instrumental period (1948–2004 CE). **c**–**j**, Composite maps for years with extremely positive (D90; north) and negative (D10; south) reconstructed EU JSL values for July–August 500 hPa geopotential height (Z500) (ref. 35) for the period 1659–1999 CE (**c**,**d**); July–August temperature[36] for 1766–2000 CE (**e**,**f**); July–August precipitation[36] for 1766–2000 CE (**g**,**h**); and June–July–August Old World Drought Atlas (OWDA) scPDSI (ref. 37) for 1300–2004 CE (**i**,**j**). In **c**–**j**, coloured composite maps are shown only where $P \leq 0.1$, and areas with statistically significant values after controlling for the false discovery rate ($\alpha_{FDR} \leq 0.1$) are cross-hatched.

Discussion

As the impacts of anthropogenic climate change continue to intensify, there is a growing interest in understanding how dynamical variability drives extreme climate events and societal impacts[6,11,17]. For example, certain summertime jet stream configurations are linked to atmospheric blocking[20,24] that contributes to the amplified heatwave trend in Europe[6], whereas other configurations can trigger compound heat waves in key breadbasket regions in the Northern Hemisphere, potentially threatening global food security[17]. Our results indicate that this relationship between jet stream position, climate and society has existed over centuries and emphasizes the association between EU JSL and extreme events.

Using the wealth of historical documents available on the European continent, we find a long-term relationship between EU-JSL-driven climate extremes and agricultural productivity (Fig. 5). These insights

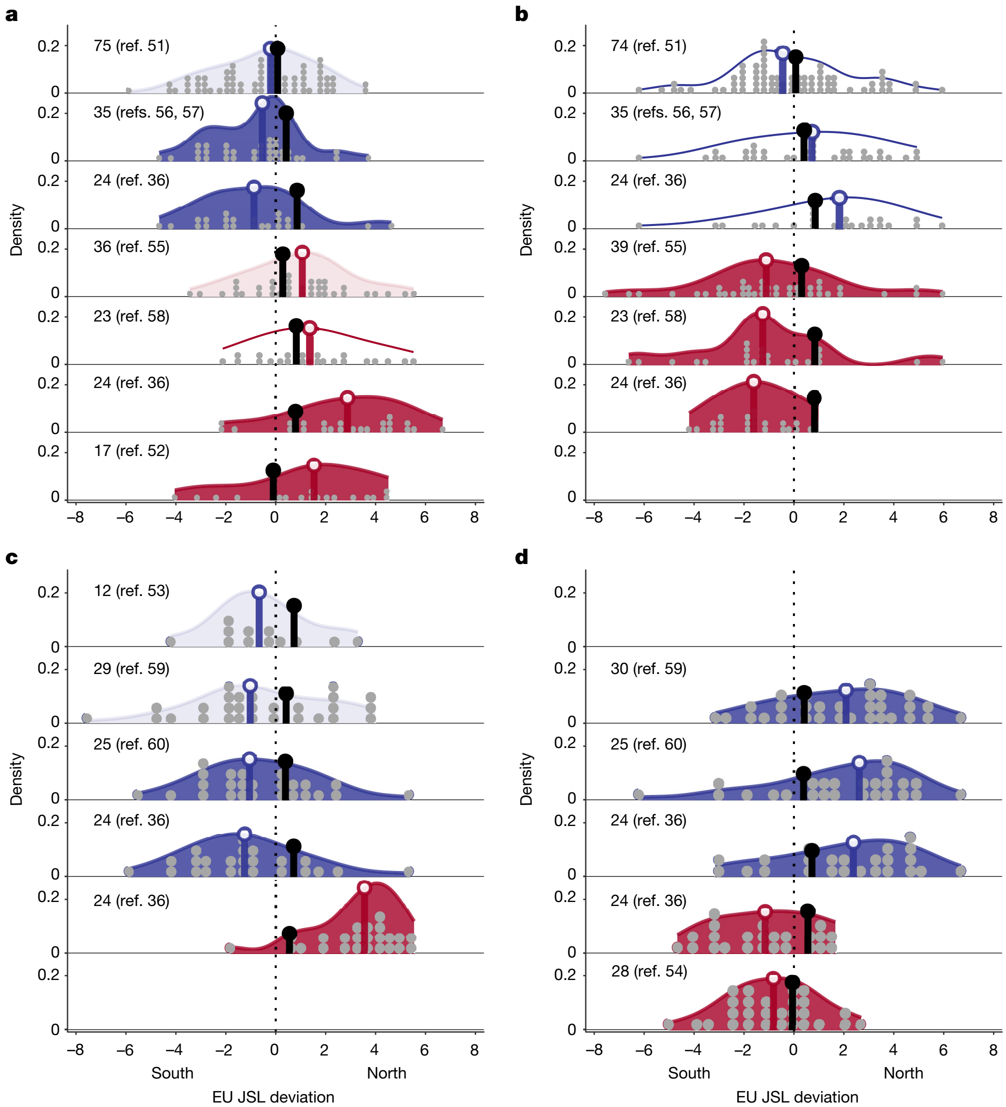

Fig. 4 | Reconstructed summer EU JSL anomalies during historical climate extreme events. a,b, Density plots of summer EU JSL deviations for historical July–August extreme hot (D90; **a**) and cold (D10; **b**) events relative to the mean summer EU JSL climatology (that is, non-extreme years; zero value shown by vertical dotted lines). **c**,**d**, The same for extreme dry (D10; **c**) and wet (D90; **d**) events (including floods). Results for NEMED are shown in red and results for BRIT are shown in blue. Statistically significant deviations, calculated using a Wilcoxon signed-rank test, are filled ($P \leq 0.05$) or translucent ($P \leq 0.1$). Vertical matchstick lines on the density plots represent the median values for reconstructed summer EU JSL during extreme (coloured) and non-extreme (black) years. A coloured matchstick line at the left of the black matchstick line indicates a summer EU JSL position further south and at the right of the black matchstick line indicates a summer EU JSL position further north compared with the EU JSL mean climatology. The grey dots indicate the distribution of EU JSL during the historical climate extreme years. The density curve was estimated by an empirical cumulative distribution function. The number of climatic extremes is shown in the figure and also listed in Extended Data Table 5 (refs. 36,51–60).

offer the prospect of improved understandings of the variable and sometimes contrasting agroeconomic fortunes observed across Europe over time. However, modern climate–harvest relationships cannot be unequivocally transferred to the past because of evolving farming and breeding practices, as well as differences in seed types and their climatic sensitivity[16,38,40]. Furthermore, the limitations of documentary data must be considered when interpreting our analysis of historical agriculture and climate[38,39]. For example, in smaller regions such as the British Isles, grain prices are not always fully representative of local harvest conditions because of storage between harvests, inter-regional grain trade[38,39] and differing regional sensitivities to drought or water excess[12]. For some important contemporary crops, such as drought-sensitive maize, no long historical records are available. For others, the climate–harvest relationships are identified in our analysis, but they are complex.

In the Mediterranean climate of NEMED, the effect of water stress and drought on wheat yield can be substantial[13], resulting in low yields during northern EU JSL summers (Figs. 2 and 5a). In temperate BRIT, wheat yields are negatively affected by excess water[13], also resulting in low yield during wet, northern EU JSL summers (Figs. 2 and 5a). These contrasting yield sensitivities in differing climates may explain why neither modern wheat yield data nor historical wheat and barley price data reflect the summer EU-JSL-induced dipole. Even in temperate regions such as BRIT, however, high temperatures can reduce grain yield through direct effects on crop development, as well as indirect, non-linear effects that increase atmospheric water demand[30]. These heat stress effects will increase under future anthropogenic warming[10].

Despite these qualifications, when compiling independent documentary datasets for NEMED and BRIT, we find significant biophysical

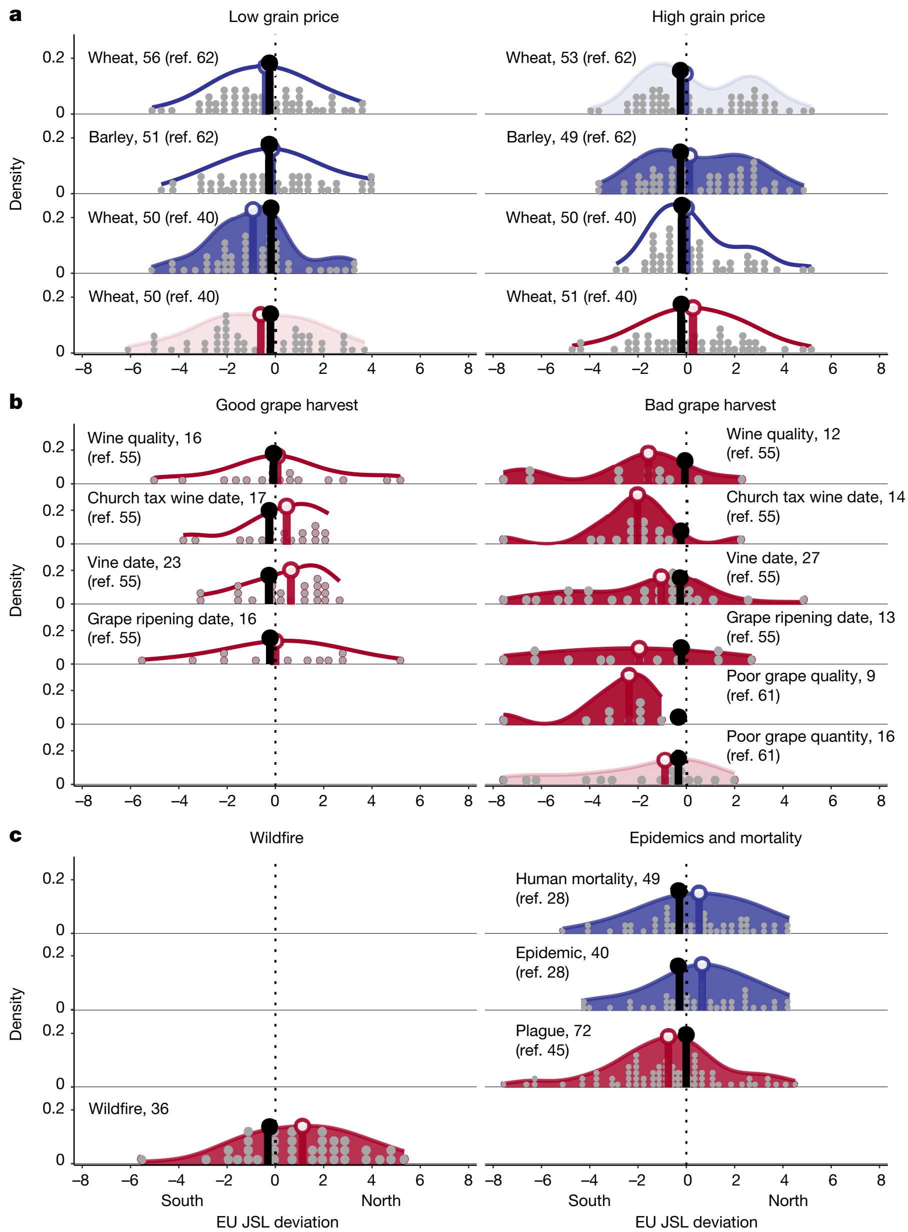

Fig. 5 | Reconstructed summer EU JSL anomalies during historical agricultural and biophysical extreme events. a, Density plots of summer EU JSL deviations for historical low (D10) and high (D90) grain price extremes relative to the mean summer EU JSL climatology (that is, non-extreme years; zero value shown by vertical dotted lines). **b**,**c**, The same for historical good (D90) and poor (D10) grape harvest years (**b**) and for biophysical events (**c**), including wildfire (left) and epidemics and human mortality (right). Results for NEMED are shown in red and results for BRIT are shown in blue. Statistically significant deviations, calculated using a Wilcoxon signed-rank test, are filled ($P \leq 0.05$) or translucent ($P \leq 0.1$). Vertical matchstick lines on the density plots represent the median values for reconstructed summer EU JSL during extreme (coloured) and non-extreme (black) years. A coloured matchstick line at the left of the black matchstick line indicates a summer EU JSL position further south and at the right of the black matchstick line indicates a summer EU JSL position further north compared with the EU JSL mean climatology. The grey dots indicate the distribution of EU JSL during the historical climate extreme years. The density curve was estimated by an empirical cumulative distribution function. The number of climatic extremes is shown in the figure and also listed in Extended Data Table 5 (refs. 28,40,45,55,61,62).

(for example, grape harvest), economic (for example, wine quality and grain price) and demographic (for example, mortality and epidemics) impacts of summer EU JSL variability (Fig. 5) that represent first- to third-order impacts in the climate–society interaction model[27,41]. The seasonality of our reconstruction probably contributes to the strength of these agricultural and societal impacts: summer is the primary growing season for grapes and maize, as well as for grain north of the Mediterranean region, and is the season when temperature variability exerts its strongest influence on historical grain prices[40]. For Mediterranean wheat and barley, cooler and wetter summers can delay plant senescence arising from (terminal) thermal and drought stress, thereby extending the grain filling period and promoting higher yields[42,43]. Summer is also, generally, the peak season for plague-related mortality because of increased flea activity and human mobility[44].

The impacts of cool and wet summers on historical crop failures[29,38,41], grain prices[40] and the emergence, intensification and diffusion of the plague and epidemics[27,28,45] have been previously documented. Our study demonstrates that EU JSL variability creates a dipole in the cool and wet summers between BRIT and NEMED that is reflected in historical epidemics and mortality patterns (Fig. 5c).

Given the complexity of climate–society interactions and the many potential interactions between societal components[29,46], the consistency of the observed association between extremes in the EU JSL spatial pattern and past biophysical, economic and demographic stressors is striking. Yet it is, nonetheless, explicable given the many known climate–societal impact pathways and the prospect of cascades and amplifying feedback. For instance, failed harvests can result in food scarcity, malnutrition and compromised immune functions, creating cascading effects through epidemics that may initiate feedback in which reduced agricultural labour prolongs or exacerbates harvest reductions[27,44]. Today, biophysical (for example, wildfires), agricultural (for example, crop production), health (for example, heat stress) and economic impacts represent major and interrelated climate risks that have been identified as priorities for European policy on climate adaptation[10]. The Russian heatwave of 2010, for instance, was primarily caused by a long-lived blocking event, linked to a northerly jet stream position and resulted in extreme wildfires, 55,000 heat-related deaths and a 25% reduction in wheat production in Russia[11,47]. By highlighting the historical link between EU JSL variability and extremes in climate, ecosystems and human systems, our results may contribute to risk assessments of cascade effects associated with future compound climate extremes[9–11].

Beyond highlighting the intricacies of these climate–societal relationships, our reconstruction shows that EU JSL variability over the past 705 years has consistently created a summertime climate dipole (Fig. 3 and Extended Data Fig. 5). Our reconstruction demonstrates the role of large-scale circulation patterns in driving extreme events over centuries in the past, as has already been demonstrated for the instrumental period[17]. This long-term record also provides a perspective that can contextualize modern interactions between EU JSL and weather extremes. Most extreme values in the instrumental period are associated with anomalously northern EU JSL positions, possibly corroborating evidence for a northward shift in the jet stream under anthropogenic warming[2]. Our results suggest that NEMED wildfire risk will increase if the EU JSL shifts northward (Fig. 5c), which could also amplify the effects of anthropogenic warming on wildfire, in line with increased fire activity in North America under northern JSL conditions[4,21]. We further find that northern EU JSL extremes can lead to major crop yield reductions at both ends of the climate dipole (Fig. 2), potentially challenging food security in Europe. Historically, northern EU JSL extremes have led to high grain prices, the spread of epidemics and above-average human mortality in BRIT (Fig. 5).

By extending the EU JSL record back to the pre-industrial era, we can also improve our understanding of its role as a driver of climate extremes under dynamic (rather than thermodynamic) forcing and help inform model development and attribution studies[4,25,48]. Most projections of future Northern Hemisphere jet stream behaviour under continued warming suggest a weak northward shift and enhanced waviness[1,2]. These projections of future jet stream behaviour are informative but uncertain because of our incomplete understanding of jet stream dynamics[49]. Records of historical EU JSL offer a long-term perspective on the frequency and intensity of atmospheric configurations that lead to extreme weather events[50]. The EU-JSL-driven summer climate dipole is an important configuration to consider for a future in which warmer temperatures and intensified summer climate extremes may exacerbate conditions on both sides of the dipole.

Online content

Any methods, additional references, Nature Portfolio reporting summaries, source data, extended data, supplementary information, acknowledgements, peer review information; details of author contributions and competing interests; and statements of data and code availability are available at https://doi.org/10.1038/s41586-024-07985-x.

1. Stendel, M., Francis, J., White, R., Williams, P. D. & Woollings, T. in *Climate Change* 3rd edn (ed. Letcher, T. M.) 327–357 (Elsevier, 2021).
2. Woollings, T., Drouard, M., O'Reilly, C. H., Sexton, D. M. H. & McSweeney, C. Trends in the atmospheric jet streams are emerging in observations and could be linked to tropical warming. *Commun. Earth Environ.* **4**, 125 (2023).
3. Galfi, V. M. & Messori, G. Persistent anomalies of the North Atlantic jet stream and associated surface extremes over Europe. *Environ. Res. Lett.* **18**, 024017 (2023).
4. Wahl, E. R., Zorita, E., Trouet, V. & Taylor, A. H. Jet stream dynamics, hydroclimate, and fire in California from 1600 CE to present. *Proc. Natl Acad. Sci. USA* **116**, 5393–5398 (2019).
5. Robinson, A., Lehmann, J., Barriopedro, D., Rahmstorf, S. & Coumou, D. Increasing heat and rainfall extremes now far outside the historical climate. *NPJ Clim. Atmos. Sci.* **4**, 45 (2021).
6. Faranda, D., Messori, G., Jezequel, A., Vrac, M. & Yiou, P. Atmospheric circulation compounds anthropogenic warming and impacts of climate extremes in Europe. *Proc. Natl Acad. Sci. USA* **120**, e2214525120 (2023).
7. Shaw, T. A. & Miyawaki, O. Fast upper-level jet stream winds get faster under climate change. *Nat. Clim. Change* **14**, 61–67 (2024).
8. Coumou, D., Petoukhov, V., Rahmstorf, S., Petri, S. & Schellnhuber, H. J. Quasi-resonant circulation regimes and hemispheric synchronization of extreme weather in boreal summer. *Proc. Natl Acad. Sci. USA* **111**, 12331–12336 (2014).
9. AghaKouchak, A. et al. Climate extremes and compound hazards in a warming world. *Annu. Rev. Earth Planet. Sci.* **48**, 519–548 (2020).
10. European Environment Agency. *The First European Climate Risk Assessment (EUCRA)* Executive Summary (European Environment Agency, 2024).
11. Balch, J. K. et al. Social-environmental extremes: rethinking extraordinary events as outcomes of interacting biophysical and social systems. *Earth's Future* **8**, e2019EF001319 (2020).
12. Beillouin, D., Schauberger, B., Bastos, A., Ciais, P. & Makowski, D. Impact of extreme weather conditions on European crop production in 2018. *Philos. Trans. R. Soc. B. Biol. Sci.* **375**, 20190510 (2020).
13. Zampieri, M., Ceglar, A., Dentener, F. & Toreti, A. Wheat yield loss attributable to heat waves, drought and water excess at the global, national and subnational scales. *Environ. Res. Lett.* **12**, 064008 (2017).
14. Zhao, C. et al. Temperature increase reduces global yields of major crops in four independent estimates. *Proc. Natl Acad. Sci. USA* **114**, 9326–9331 (2017).
15. Sah, R. P. et al. Impact of water deficit stress in maize: phenology and yield components. *Sci. Rep.* **10**, 2944 (2020).
16. Helman, D. & Bonfil, D. J. Six decades of warming and drought in the world's top wheat-producing countries offset the benefits of rising CO_2 to yield. *Sci. Rep.* **12**, 7921 (2022).
17. Kornhuber, K. et al. Risks of synchronized low yields are underestimated in climate and crop model projections. *Nat. Commun.* **14**, 3528 (2023).
18. Mahlstein, I., Martius, O., Chevalier, C. & Ginsbourger, D. Changes in the odds of extreme events in the Atlantic basin depending on the position of the extratropical jet. *Geophys. Res. Lett.* **39**, L22805 (2012).
19. Belmecheri, S., Babst, F., Hudson, A. R., Betancourt, J. & Trouet, V. Northern Hemisphere jet stream position indices as diagnostic tools for climate and ecosystem dynamics. *Earth Interact.* **21**, 1–23 (2017).
20. Dorado-Liñán, I. et al. Jet stream position explains regional anomalies in European beech forest productivity and tree growth. *Nat. Commun.* **13**, 2015 (2022).
21. Jain, P. & Flannigan, M. The relationship between the polar jet stream and extreme wildfire events in North America. *J. Clim.* **34**, 6247–6265 (2021).
22. Lehmann, J. & Coumou, D. The influence of mid-latitude storm tracks on hot, cold, dry and wet extremes. *Sci Rep.* **5**, 17491 (2015).
23. Trouet, V., Babst, F. & Meko, M. Recent enhanced high-summer North Atlantic Jet variability emerges from three-century context. *Nat. Commun.* **9**, 180 (2018).
24. Brunner, L., Schaller, N., Anstey, J., Sillmann, J. & Steiner, A. K. Dependence of present and future European temperature extremes on the location of atmospheric blocking. *Geophys. Res. Lett.* **45**, 6311–6320 (2018).
25. Weiland, R. S., van der Wiel, K., Selten, F. & Coumou, D. Intransitive atmosphere dynamics leading to persistent hot-dry or cold-wet European summers. *J. Clim.* **34**, 1–48 (2021).
26. Gagen, M. H. et al. North Atlantic summer storm tracks over Europe dominated by internal variability over the past millennium. *Nat. Geosci.* **9**, 630–635 (2016).
27. Ljungqvist, F. C., Seim, A. & Huhtamaa, H. Climate and society in European history. *WIREs Clim. Change* **12**, e691 (2021).
28. Campbell, B. M. & Ludlow, F. Climate, disease and society in late-medieval Ireland. *Proc. R. Ir. Acad. Archaeol. Culture Hist. Lit.* **120C**, 159–252 (2020).
29. Camenisch, C. et al. The 1430s: a cold period of extraordinary internal climate variability during the early Sporer Minimum with social and economic impacts in north-western and central Europe. *Clim. Past* **12**, 2107–2126 (2016).
30. Webber, H. et al. Diverging importance of drought stress for maize and winter wheat in Europe. *Nat. Commun.* **9**, 4249 (2018).
31. Rydval, M. et al. Reconstructing 800 years of summer temperatures in Scotland from tree rings. *Clim. Dyn.* **49**, 2951–2974 (2017).
32. Büntgen, U., Frank, D. C., Nievergelt, D. & Esper, J. Summer temperature variations in the European Alps, A.D. 755–2004. *J. Clim.* **19**, 5606–5623 (2006).
33. Wanner, H., Pfister, C. & Neukom, R. The variable European Little Ice Age. *Quat. Sci. Rev.* **287**, 107531 (2022).
34. Luterbacher, J. & Pfister, C. The year without a summer. *Nat. Geosci.* **8**, 246–248 (2015).
35. Luterbacher, J. et al. Reconstruction of sea level pressure fields over the Eastern North Atlantic and Europe back to 1500. *Clim. Dyn.* **18**, 545–561 (2002).
36. Casty, C., Raible, C. C., Stocker, T. F., Wanner, H. & Luterbacher, J. A European pattern climatology 1766–2000. *Clim. Dyn.* **29**, 791–805 (2007).
37. Cook, E. R. et al. Old World megadroughts and pluvials during the Common Era. *Sci. Adv.* **1**, e1500561 (2015).
38. Ljungqvist, F. C. et al. Climatic signatures in early modern European grain harvest yields. *Clim. Past* **19**, 2463–2491 (2023).

39. Esper, J. et al. Environmental drivers of historical grain price variations in Europe. *Clim. Res.* **72**, 39–52 (2017).
40. Ljungqvist, F. C. et al. The significance of climate variability on early modern European grain prices. *Cliometrica* **16**, 29–77 (2022).
41. Pfister, C. & Wanner, H. *Climate and Society in Europe: The Last Thousand Years* (Haupt, 2021).
42. Rharrabti, Y., Villegas, D., Royo, C., Martos-Núñez, V. & García del Moral, L. F. Durum wheat quality in Mediterranean environments: II. Influence of climatic variables and relationships between quality parameters. *Field Crops Res.* **80**, 133–140 (2003).
43. Yang, C., Fraga, H., van Ieperen, W. & Santos, J. A. Assessing the impacts of recent-past climatic constraints on potential wheat yield and adaptation options under Mediterranean climate in southern Portugal. *Agric. Syst.* **182**, 102844 (2020).
44. Campbell, B. M. *The Great Transition: Climate, Disease and Society in the Late-Medieval World* (Cambridge Univ. Press, 2016).
45. Büntgen, U., Ginzler, C., Esper, J., Tegel, W. & McMichael, A. J. Digitizing historical plague. *Clin. Infect. Dis.* **55**, 1586–1588 (2012).
46. Degroot, D. et al. Towards a rigorous understanding of societal responses to climate change. *Nature* **591**, 539–550 (2021).
47. Barriopedro, D., Fischer, E. M., Luterbacher, J., Trigo, R. M. & García-Herrera, R. The hot summer of 2010: redrawing the temperature record map of Europe. *Science* **332**, 220–224 (2011).
48. Williams, A. P. et al. Large contribution from anthropogenic warming to an emerging North American megadrought. *Science* **368**, 314–318 (2020).
49. Sun, X. et al. Enhanced jet stream waviness induced by suppressed tropical Pacific convection during boreal summer. *Nat. Commun.* **13**, 1288 (2022).
50. Van Oldenborgh, G. J. et al. Attributing and projecting heatwaves is hard: we can do better. *Earths Future* **10**, e2021EF002271 (2022).
51. van Engelen, A. F. V., Buisman, J. & Ijnsen, F. in *History and Climate: Memories of the Future?* (eds Jones, P. D. et al.) 101–124 (Springer, 2001).
52. Camuffo, D. et al. 500-Year temperature reconstruction in the Mediterranean Basin by means of documentary data and instrumental observations. *Clim. Change* **101**, 169–199 (2010).
53. Cole, G. A. & Marsh, T. J. in *Climate Variability and Change: Hydrological Impacts* (eds Demuth, S. et al.) Vol. 308, 483–489 (2006).
54. Pavese, M. P., Banzon, V., Colacino, M., Gregori, G. P. & Pasqua, M. in *Climate Since AD 1500* (eds Bradley, R. S. & Jones, P. D.) 155–170 (Routledge, 1992).
55. Kiss, A., Wilson, R. & Bariska, I. An experimental 392-year documentary-based multi-proxy (vine and grain) reconstruction of May-July temperatures for Koszeg, West-Hungary. *Int. J. Biometeorol.* **55**, 595–611 (2011).
56. Manley, G. Central England temperatures: monthly means 1659 to 1973. *Q. J. R. Meteorol. Soc.* **100**, 389–405 (1974).
57. Parker, D. & Horton, B. Uncertainties in central England temperature 1878-2003 and some improvements to the maximum and minimum series. *Int. J. Climatol.* **25**, 1173–1188 (2005).
58. Böhm, R. et al. The early instrumental warm-bias: a solution for long central European temperature series 1760–2007. *Clim. Change* **101**, 41–67 (2010).
59. Murphy, C. et al. A 305-year continuous monthly rainfall series for the island of Ireland (1711–2016). *Clim. Past* **14**, 413–440 (2018).
60. Alexander, L. V. & Jones, P. D. Updated precipitation series for the U.K. and discussion of recent extremes. *Atmos. Sci. Lett.* **1**, 142–150 (2001).
61. Rácz, L. Carpathian Basin – the winner of the Little Ice Age climate changes: long-term time-series analysis of grain, grape and hay harvests between 1500 and 1850. *Econ. Ecohist.* **16**, 81–96 (2020).
62. Clark, G. in *Research in Economic History* Vol. 22, 41–123 (Emerald, 2004).

Methods

Jet stream latitude calculations

Our target for reconstruction is the second mode of interannual summer JSL variability over the EU domain (30° W–40° E). This mode of EU JSL explains about 26% of its variability and represents JSL variability over Central and Eastern Europe (5° W–40° E; Fig. 1a,b and Extended Data Fig. 1), whereas the first mode represents JSL variability primarily over Western Europe[20] and is not a focus of this study. To calculate the target time series for summer EU JSL variability, we defined monthly JSL as the latitude of maximum average monthly 300 hPa zonal wind speed for each 2.5° longitudinal window from 30° W–40° E for latitudes from 20° N–90° N (refs. 63–66). This analysis is based on the monthly scalar zonal wind data from the National Centers for Environmental Prediction/National Center for Atmospheric Research (NCEP/NCAR) globally gridded reanalysis dataset[67] (NCEP/NCAR Reanalysis 1, 2.5° × 2.5° resolution; 1948–2018 CE). We then averaged monthly JSL data for each longitude for July and August, the period in which our tree-ring chronologies are generally most sensitive to temperature variability (Extended Data Table 2). Next, we performed a principal components analysis (PCA) for the July–August EU JSL time series (Extended Data Fig. 1) and used the resulting PC2 time series (EU JSL) as our target for reconstruction. Positive EU JSL values indicate that the JSL is further north with respect to the mean climatology over Central and Eastern Europe, whereas negative values indicate a southern position (Fig. 1a,b).

To explore the relationship between interannual variability in observed summer EU JSL and regional climate, we conducted field Pearson correlation analyses between the July–August EU JSL time series and July–August geopotential height at 500 hPa (Z500) from the NCEP/NCAR reanalysis[67], July–August temperature, precipitation and the scPDSI from the Climatic Research Unit (CRU) ts4.05 datasets[68] (Extended Data Fig. 2). We completed these correlation analyses for the common period covered by both the CRU climate data and the NCEP/NCAR reanalysis (1948–2018 CE) using the KNMI Climate Explorer[69] (https://climexp.knmi.nl/correlate.cgi).

Apart from the field correlation analyses, we conducted a composite analysis of the reconstructed gridded climate data during northern and southern summer EU JSL extremes (Fig. 1). We used the peak-over-threshold method[70] to select extremes in the summer EU JSL time series. We defined extreme positive EU JSL years as higher than the 80th percentile (D80) and negative EU JSL years as lower than the 20th percentile (D20) over the instrumental period (1948–2018 CE; Extended Data Table 1). In these field correlation and composite analyses, we use the Benjamini–Hochberg false discovery rate (FDR) correction for P-values to mitigate the increase in false positives from multiple testing[71]. We set $\alpha_{\mathrm{FDR}} = 0.1$ to maintain a global α level of 0.05 (ref. 72). The P_{FDR} was estimated as follows:

$$P_{\mathrm{FDR}} = \max_{j=1,\ldots,k}[P_j : P_j \leq (j/N)\alpha_{\mathrm{FDR}}] \quad (1)$$

where α_{FDR} is the control level for FDR, P_j is the P-value of the jth local test after sorting P-values in an ascending order and N is the total number of local tests. Grid cells with P-values of local test less than P_{FDR} are considered significant.

Agricultural productivity

To quantify the influence of summer EU JSL variability on crop yield, we created composite maps for our two regions of interest (BRIT: 50° N–60° N and 10° W–5° E and NEMED: 35° N–50° N and 10° E–30° E; Fig. 2) from the Global Dataset of Historical Yield (GDHY), a gridded (0.5° × 0.5°) annual dataset for 1981–2016 CE that includes maize (NEMED only) and wheat yields[73]. Composites were created for the northern and southern extreme (D80 and D20) summer EU JSL years (Fig. 2).

We also obtained annual crop yield data from the Food and Agriculture Organization of the United Nations (https://www.fao.org/faostat/en/#data/QCL), which covers the period from 1961 CE to 2021 CE. Historical documentary yield and phenological records are available for grapes and historical grain price series are available for wheat and barley (Extended Data Table 5), making it possible, with caution, to compare modern and historical results. We selected the crop yield data of the Food and Agriculture Organization for the UK, Ireland and the Netherlands (BRIT) and for Bulgaria, Albania, Greece and Italy (NEMED). For BRIT maize, data spanning the entire period of the dataset were only available for the Netherlands. For each country, we applied a 20-year smoothing spline detrending method to the annual crop yield data, using the ratio between the raw crop yield values and fitted values to remove trends unrelated to climate, such as those pertaining to agricultural management and fertilization[14,16]. We then pooled these country-scale crop yield data per region to examine the influence of EU JSL extremes on regional crop yield variability (Extended Data Fig. 3). We used D80 and D20 (northern and southern) EU JSL positions from 1961 to 2018 CE as extreme event years in the comparison (Fig. 2).

To emphasize the influence of EU JSL extremes on crop yield during the instrumental period, we compared the difference in crop yield during northern and southern (D80 and D20) EU JSL extremes using a Wilcoxon signed-rank test (Extended Data Figs. 3 and 6). To equalize the size of the groups, we randomly resampled the larger groups several times to get a representative downsized group matching the size of the smallest one.

Regional tree-ring proxy records

To reconstruct interannual variability in July–August EU JSL, we combined annually resolved tree-ring records that are sensitive to summer temperature from three European regions in which summer climate is influenced by summer EU JSL variability (Fig. 1 and Extended Data Table 2). Two of the chronologies (BRIT and ALP) have been previously published[31,32], and we complemented these with a newly developed chronology from NEMED. To keep a highly replicated series (more than 20 samples) with robust expressed population signal (EPS; ≥0.85) (refs. 74,75), we limited our analysis of the BRIT chronology to start at 1300 CE, because replicated series and EPS are lower from 1200 to 1299 CE (fig. 1 of ref. 31). The ALP and NEMED chronologies are based on maximum latewood density (MXD), whereas the BRIT chronology is based on a low-frequency (low-pass-filtered) tree-ring width (RW) chronology combined with a high-frequency (high-pass-filtered) blue intensity (BI) chronology to minimize the signal of forest disturbance in the final chronology[31]. Specifically, the BRIT samples were collected from living and subfossil pine wood in central Scotland[31], which contains disturbance-related growth release due to centuries of woodland exploitation. A disturbance-corrected RW dataset was created to address this issue and to reconstruct historical temperature variability[31,76]. This involved detrending the RW data from living material using the signal-free procedure[77] with either a negative exponential or linear function, whereas subfossil RW data were detrended using a regional curve standardization approach (RCS)[78] to preserve low-frequency variability. The detrended RW series were then scaled to the 1720–1897 CE reference period and combined into a single chronology[31]. Similar to RW, both the living and subfossil BI series were separately detrended using linear regression functions and rescaled for the period 1720–1897 CE before averaging into a single BI series. A temperature reconstruction may suffer from potential low-frequency biases based only on BI (ref. 31). The final BRIT chronology integrates high-frequency variability from the BI series with low-frequency variability from the RW series[31]. BRIT chronology showed a strong summer (July–August) temperature signal consistent across a vast spatial scale, including the British Isles, parts of western Europe, Scandinavia and the northern Iberian Peninsula[31].

We used the published ALP (ref. 32) and BRIT (ref. 31) reconstructions in our analysis, including the original detrending methods (RCS) used in those studies. For the NEMED chronology, we combined newly developed *Pinus heldreichii* MXD measurements from Lura National Park in Albania (41.48° N, 20.14° E, 1,900 m above sea level (a.s.l.); 75 series) and the Pirin Mountains in Bulgaria (41.42° N, 23.30° E, 2,150 m a.s.l.; 93 series)[79] with existing *P. heldreichii* MXD time series from Mount Smolikas (192 series)[80,81] and Mount Olympus (65 series)[82] in Greece. We combined all 425 individual tree-ring series into a single file and performed a COFECHA-based cross-dating quality test[83,84] to develop a NEMED master chronology that extends back to 1200 CE. We removed age-related trends from individual series using RCS (refs. 78,85,86). To address differences in absolute wood density values between different tree sizes and measurement setups[74], we transformed each contributing MXD series into *z*-scores before combining individual series into the NEMED chronology by averaging the detrended series using a biweight robust mean[87] in the R package dplR (ref. 88). Finally, we truncated the NEMED chronology based on an EPS threshold of 0.85 (refs. 75,86) (Extended Data Fig. 7a).

To assess the summer temperature sensitivity of the chronologies, we correlated each chronology with an instrumental time series of July–August temperature, derived from the CRU ts4.05 gridded dataset[68]. We averaged gridded temperature time series for the 2° × 2° grid cells surrounding the location of each chronology and calculated Pearson correlation coefficients starting in 1901 CE through the most recent year of each chronology (Extended Data Table 2). To investigate chronology–temperature relationships at different frequency domains, we calculated correlation coefficients for both the unfiltered and high-pass-filtered time series, in which the high-pass filter was calculated as the difference between the current year and the previous year.

Before reconstructing summer EU JSL variability, the primary dynamic driver of summer temperature variability, we removed the thermodynamic effects of rising post-industrial greenhouse gas (GHG) emissions[89] from our chronologies. To achieve this, we assumed that recent, centennial-length large-scale (for example, across the extra-tropical Northern Hemisphere) temperature trends are primarily caused by GHG forcing, whereas regional residuals are primarily related to the dynamical component. We averaged annual temperature variability for the 1901–2018 CE period over the extra-tropical Northern Hemisphere using the CRU ts4.05 dataset (Extended Data Fig. 7b). We then decomposed both this large-scale temperature time series and each of the tree-ring chronologies into low- and high-frequency time series using a 100-year loess smoothing method and established an empirical relationship between the low-frequency temperature and tree-ring time series (Extended Data Fig. 7c). We then adjusted the low-frequency time series of the tree-ring chronologies using the residuals of the empirical model (that is, the original low-frequency time series minus the empirically modelled values)[90]. This procedure removes the low-frequency trend over the post-industrial period (1901–present), presumed to be caused by rising GHG, not by EU JSL variability from the chronologies (Extended Data Fig. 7d,e). Finally, we combined the adjusted low-frequency and original high-frequency time series of the chronologies to create the final, adjusted chronologies (Extended Data Fig. 7f).

EU JSL reconstruction

To reconstruct summer EU JSL variability, we used a stepwise multiple linear regression (MLR) model (Extended Data Table 3) with summer EU JSL as the reconstruction target (dependent variable) and the three adjusted regional tree-ring chronologies as the predictor variables (independent variables). We used the adjusted R-square (R^2_{adj}), an *F*-test and Akaike information criterion (AIC) parameters to evaluate the MLR models as each predictor entered the model. The residuals from the final MLR model expressed a normal distribution with no trend (Extended Data Fig. 4a,b). The residuals were homoscedastic and no outliers were detected using Cook's distance index (Extended Data Fig. 4c,d). We evaluated the reconstruction skill based on reduction of error (RE), coefficient of efficiency (CE) (ref. 86) and R^2_{adj} over two periods of equal length covering the common period between our reanalysis-based target and the chronologies (1948–1975 CE and 1976–2004 CE) (Extended Data Table 3b). Our calibration and verification trials show that summer EU JSL can be skillfully reconstructed back to 1300 CE (1300–2004 CE), with 36–41% of the variance explained in the verification period and positive RE and CE statistics. Finally, we scaled the reconstruction to fit the mean and variance of the summer EU JSL target over the period of overlap (1948–2004 CE) and estimated uncertainty in the reconstruction based on the calibration uncertainty using the 95% prediction interval derived from the MLR of the reconstruction against the target (Fig. 3a,b). We further calculated the correlation coefficients between the reconstructed and instrumental summer EU JSL at high and low frequencies using a 20-year smoothing spline to high- and low-pass filter series, respectively (Extended Data Fig. 4c). We also conducted a cross-wavelet coherency analysis between the instrumental and reconstructed summer EU JSL to evaluate coherence in their variability[88,91] (Extended Data Fig. 4d).

Reconstructed EU JSL field correlations

To place the relationship between summer EU JSL variability and regional climate in a centennial-scale context, we conducted spatial Pearson correlation and composite analyses between our summer EU JSL reconstruction and independent gridded climate reconstruction fields (Fig. 3 and Extended Data Fig. 5). These climate field reconstructions include July–August Z500 (1659–1999 CE) (ref. 35), July–August temperature (1766–2000 CE) (ref. 36), July–August precipitation (1766–2000 CE) (ref. 36) and June–July–August scPDSI data from the Old World Drought Atlas (OWDA) (800–2012 CE) (ref. 37). We tested the significance of the correlations for each grid point for their maximum period of overlap by controlling the false discovery rate at $\alpha_{FDR} \le 0.1$. We conducted these spatial correlation analyses for the entire period of overlap, as well as for three sub-periods: 1701–1800, 1801–1900 and 1901–2000 CE (Extended Data Fig. 5). For scPDSI, the correlation analysis for the most recent period extends to 2004 CE. For Z500, the analysis for the oldest period extends back to 1659 CE. For temperature and precipitation, the analysis for the oldest period is truncated and begins at 1766 CE.

Reconstructed summer EU JSL impacts

To analyse the climatic conditions over Europe during reconstructed summer EU JSL extremes, we used the peak-over-threshold method[70] to select extremes in the summer EU JSL reconstruction. We defined extreme positive years as those with D90 EU JSL and extreme negative years as those with D10 EU JSL over the entire reconstruction (1300–2004 CE; 71 positive and 71 negative extremes; Extended Data Table 4). We then conducted a composite analysis with the aforementioned reconstructed gridded climate data during the positive and negative summer EU JSL extremes (Fig. 3c–j).

To investigate EU JSL anomalies during past European climate extremes, we compared historical summer EU JSL positions during event years characterized by extreme climate, natural hazards and societal extremes with those of non-extreme years (Figs. 4 and 5 and Extended Data Table 5) using the Wilcoxon signed-rank test for each included dataset. In all cases, we equalized the sizes of the groups (D90, D10 and non-extreme) by resampling the larger groups several times to get a representative downsized group matching the size of the smallest one. We extracted climate extreme event years for two sub-regions (BRIT: 11° W–3° E, 49° N–59° N and NEMED: 15° E–30° E, 40° N–45° N) from the reconstructed temperature and precipitation gridded fields[36] (Fig. 4a,b). For each time series, we defined extreme years as higher than D90 and lower than D10 over the entire reconstruction period. We complemented these gridded-data-based climate extreme event series with four continuous summer temperature records and two continuous precipitation records that are based on instrumental and/or documentary datasets from BRIT and NEMED (Extended Data

Table 5). Event years in the continuous series were defined based on the D90 and D10 values. For the summer temperature data in ref. 51, we used the Category III cluster (warm summer; $n = 75$) as hot events and the Category I cluster (cool summer, $n = 74$) (from table 5 of ref. 51) as cold events, using only the most recent year of these multi-year extreme events in our analysis (Extended Data Table 5). We further compiled one independent, discrete temperature and two independent, discrete precipitation reconstructions (Extended Data Table 5). Hot extremes in ref. 52 (NEMED) records were defined as years with the hottest summers in Northern–Central Italy, Southern Italy and/or Greece (from table 5 of ref. 52). Dry extremes in the discrete BRIT record were defined as years with the highest calculated aridity index in England and Wales (from fig. 2 of ref. 53).

We further extracted natural hazards (wildfires and floods) and harvest event datasets from a variety of sources (Extended Data Table 5). We compiled a NEMED wildfire event dataset by combining all fire years recorded in tree-ring-based fire-scar records from Greece[92], Bulgaria[93] and western Turkey[94] into a single list of event years. We excluded fires that occurred more recently than 1940 CE, because in these more recent years, events such as the Second World War (1940–1945) battles, the establishment of forest services and land-use changes have left a strong human (non-climate-related) fingerprint on recent wildfires in the region[92]. All flood datasets were based on discrete instrumental or documentary BRIT or NEMED datasets (Extended Data Table 5). For NEMED floods, we combined all years when floods occurred in several locations in Northern Italy (tables 1–3 of ref. 54) in June–October into a single list of event years.

To analyse good and bad harvest years, we compiled discrete (all years of catastrophic grape quantity)[61], as well as D10 and D90 values of continuous NEMED grape harvest datasets, including wine quality, vine harvest dates, church tithe (tax) wine harvest data and grape ripening dates[55]. For the wine quality data[55], we selected the categories 'very good' as a good harvest and 'very bad' as a bad harvest (Extended Data Table 5). We complemented the grape harvest data with grain price data for both NEMED and BRIT. For BRIT, we examined price data from London (wheat and barley)[62], and for NEMED, we used data from Italy and the peripheral cluster region for wheat in ref. 40. To account for large step shifts in the continuous grain price data time series, assumed to result from factors not related to climate, we calculated D90 and D10 values for each 50-year period ($n = 5$ for each period) of the time series. We then compiled a dataset of high grain price (reflecting bad harvest) extreme events as the list of all D90 years and a dataset of low grain price (reflecting good harvest) extreme events as the list of all D10 years (Extended Data Table 5). We further compared the difference in grape harvest during northern and southern (D90 and D10 for the historical period and D80 and D20 for the instrumental period) EU JSL extremes using a Wilcoxon signed-rank test[95] (Extended Data Fig. 6).

To analyse the potential relationships between summer EU JSL variability and past societal disruptions, we used datasets on epidemics and mortality (Fig. 5c) over the maximum period of overlap between the two datasets (Extended Data Table 5). For BRIT epidemics and human mortality, we used discrete documentary datasets from Ireland compiled in ref. 28. We derived a NEMED plague dataset by extracting NEMED (38° N–46° N; 13° E–23° E; Fig. 1a) plague events from ref. 45. We defined NEMED plague events as years when three or more plague outbreaks occurred, which corresponds to the D90 value.

Data availability

All reconstructed and instrumental EU JSL datasets can be found at Zenodo (https://doi.org/10.5281/zenodo.13120683)[96] and are freely available at the NOAA National Centers for Environmental Information (NCEI). The reconstructed summer EU JSL can be found in the NOAA Paleoclimatology Database. The NCEP/NCAR data can be found at https://psl.noaa.gov/. The Climatic Research Unit CRUts temperature data can be found at https://catalogue.ceda.ac.uk/uuid/10d3e3640f004c578403419aac167d82. The ALP and BRIT temperature reconstructions can be found at the NCEI/NOAA International Tree-Ring Data Bank at https://www.ncei.noaa.gov/products/paleoclimatology/tree-ring.

Code availability

The code used in this study can be found at Zenodo (https://doi.org/10.5281/zenodo.13120683)[96].

63. Barton, N. P. & Ellis, A. W. Variability in wintertime position and strength of the North Pacific jet stream as represented by re-analysis data: winter North Pacific jet stream variability. *Int. J. Climatol.* **29**, 851–862 (2009).
64. Woollings, T., Hannachi, A. & Hoskins, B. Variability of the North Atlantic eddy-driven jet stream. *Q. J. R. Meteorol. Soc.* **136**, 856–868 (2010).
65. Harnik, N., Galanti, E., Martius, O. & Adam, O. The anomalous merging of the African and North Atlantic jet streams during the Northern Hemisphere winter of 2010. *J. Clim.* **27**, 7319–7334 (2014).
66. Lachmy, O. & Harnik, N. Wave and jet maintenance in different flow regimes. *J. Atmos. Sci.* **73**, 2465–2484 (2016).
67. Kalnay, E. et al. The NCEP/NCAR 40-year reanalysis project. *Bull. Am. Meteor. Soc.* **77**, 437–472 (1996).
68. Harris, I., Osborn, T. J., Jones, P. & Lister, D. Version 4 of the CRU TS monthly high-resolution gridded multivariate climate dataset. *Sci. Data* **7**, 109 (2020).
69. Trouet, V. & Van Oldenborgh, G. J. KNMI Climate Explorer: a web-based research tool for high-resolution paleoclimatology. *Tree-Ring Res.* **69**, 3–13 (2013).
70. Engeland, K., Hisdal, H. & Frigessi, A. Practical extreme value modelling of hydrological floods and droughts: a case study. *Extremes* **7**, 5–30 (2005).
71. Benjamini, Y. & Hochberg, Y. Controlling the false discovery rate: a practical and powerful approach to multiple testing. *J. R. Stat. Soc B* **57**, 289–300 (1995).
72. Wilks, D. S. "The Stippling Shows Statistically Significant Grid Points": how research results are routinely overstated and overinterpreted, and what to do about it. *Bull. Am. Meteor. Soc.* **97**, 2263–2273 (2016).
73. Iizumi, T. & Sakai, T. The global dataset of historical yields for major crops 1981–2016. *Sci. Data* **7**, 97 (2020).
74. Esper, J., Düthorn, E., Krusic, P. J., Timonen, M. & Büntgen, U. Northern European summer temperature variations over the Common Era from integrated tree-ring density records: Northern European common era summer temperatures. *J. Quat. Sci.* **29**, 487–494 (2014).
75. Wigley, T. M. L., Briffa, K. R. & Jones, P. D. On the average value of correlated time series, with applications in dendroclimatology and hydrometeorology. *J. Clim. Appl. Meteorol.* **23**, 201–213 (1984).
76. Rydval, M., Druckenbrod, D., Anchukaitis, K. J. & Wilson, R. Detection and removal of disturbance trends in tree-ring series for dendroclimatology. *Can. J. Forest Res.* **46**, 387–401 (2016).
77. Melvin, T. M. & Briffa, K. R. A "signal-free" approach to dendroclimatic standardisation. *Dendrochronologia* **26**, 71–86 (2008).
78. Briffa, K. R. & Melvin, T. M. in *Dendroclimatology: Progress and Prospects* (eds Hughes, M. K.) 113–145 (Springer, 2011).
79. Trouet, V., Panayotov, M. P., Ivanova, A. & Frank, D. A pan-European summer teleconnection mode recorded by a new temperature reconstruction from the northeastern Mediterranean (AD 1768–2008). *Holocene* **22**, 887–898 (2012).
80. Esper, J. et al. Eastern Mediterranean summer temperatures since 730 CE from Mt. Smolikas tree-ring densities. *Clim. Dyn.* **54**, 1367–1382 (2020).
81. Klippel, L. et al. A 1200+ year reconstruction of temperature extremes for the northeastern Mediterranean region. *Int. J. Climatol.* **39**, 2336–2350 (2019).
82. Klesse, S., Ziehmer, M., Rousakis, G., Trouet, V. & Frank, D. Synoptic drivers of 400 years of summer temperature and precipitation variability on Mt. Olympus, Greece. *Clim. Dyn.* **45**, 807–824 (2015).
83. Holmes, R. L. Computer-assisted quality control in tree-ring dating and measurement. *Tree-Ring Bull.* **43**, 69–78 (1983).
84. Trouet, V. A tree-ring based late summer temperature reconstruction (AD 1675–1980) for the Northeastern Mediterranean. *Radiocarbon* **56**, S69–S78 (2014).
85. Helama, S., Melvin, T. M. & Briffa, K. R. Regional curve standardization: state of the art. *Holocene* **27**, 172–177 (2017).
86. Cook, E. R. & Kairiukstis, L. A. *Methods of Dendrochronology: Applications in the Environmental Sciences* (Kluwer Academic, 1990).
87. Cook, E. R. & Peters, K. Calculating unbiased tree-ring indices for the study of climatic and environmental change. *Holocene* **7**, 361–370 (1997).
88. Bunn, A. G. Statistical and visual crossdating in R using the dplR library. *Dendrochronologia* **28**, 251–258 (2010).
89. Deser, C., Terray, L. & Phillips, A. S. Forced and internal components of winter air temperature trends over North America during the past 50 Years: mechanisms and implications. *J. Clim.* **29**, 2237–2258 (2016).
90. Gagen, M. et al. Exorcising the 'segment length curse': summer temperature reconstruction since AD 1640 using non-detrended stable carbon isotope ratios from pine trees in northern Finland. *Holocene* **17**, 435–446 (2007).
91. Torrence, C. & Compo, G. P. A practical guide to wavelet analysis. *Bull. Am. Meteor. Soc.* **79**, 61–78 (1998).
92. Christopoulou, A., Fulé, P. Z., Andriopoulos, P., Sarris, D. & Arianoutsou, M. Dendrochronology-based fire history of *Pinus nigra* forests in Mount Taygetos, Southern Greece. *For. Ecol. Manage.* **293**, 132–139 (2013).
93. Vasileva, P. & Panayotov, M. Dating fire events in *Pinus heldreichii* forests by analysis of tree ring cores. *Dendrochronologia* **38**, 98–102 (2016).

94. Şahan, E. A. et al. Fire history of *Pinus nigra* in Western Anatolia: a first dendrochronological study. *Dendrochronologia* **69**, 125874 (2021).
95. Rey, D. & Neuhäuser, M. in *International Encyclopedia of Statistical Science* (ed. Lovric, M.) (Springer, 2011).
96. Xu, G., Broadman, E., Dorado-Liñán, I., & Trouet, V. Jet stream controls on European climate and agriculture since 1300 CE, *Zenodo*, V1, https://doi.org/10.5281/zenodo.13120683 (2024).

Acknowledgements This study was supported by the Career Foundation from the Shaanxi Province and Northwest University, the programme of Light of West China Program of the Chinese Academy of Sciences to G.X., US National Science Foundation (NSF) CAREER grant AGS-1349942 to V.T., by funding from the Spanish Programa de Ayudas Beatriz Galindo, Secretaría de Estado de Universidades, Investigación, Desarrollo e Innovación (BG20/00065), Proyectos de Generación de Conocimiento 2021, Agencia Estatal de Investigación (PID2021-128759OA-I00) and Ayudas para Incentivar la Consolidación Investigadora (CNS2022-135228) to I.D.-L. and by the Swedish Research Council (grant nos. 2018-01272 and 2023-00605) to A.S. and F.C.L.; F.L. was supported by a European Research Council (ERC) Synergy Grant (4-OCEANS; grant agreement no. 951649). We are grateful to everyone who was involved in the development of the individual tree-ring datasets and to the numerous researchers who made their data available through the International Tree-Ring Data Bank (ITRDB). We also thank NOAA/OAR/ESRL PSL, Boulder, Colorado, for providing the NCEP/NCAR Reanalysis data.

Author contributions G.X. and V.T. designed the study with input from E.B., I.D.-L., L.K., M.M., A.S., F.C.L., J.E. and R.W.; L.K., M.M., M.P., C.H., J.E., B.G., U.B., R.W. and V.T. developed the tree-ring data; G.X., E.B., I.D.-L., L.K., M.M., F.L. and V.T. analysed the data; and G.X., E.B., V.T., I.D.-L. and M.M. wrote the paper with input from all other authors. All authors contributed to the discussion and interpretation.

Competing interests The authors declare no competing interests.

Additional information
Correspondence and requests for materials should be addressed to Valerie Trouet.
Peer review information *Nature* thanks Martín Hadad, Fernando Martinez-Moreno and the other, anonymous, reviewer(s) for their contribution to the peer review of this work.

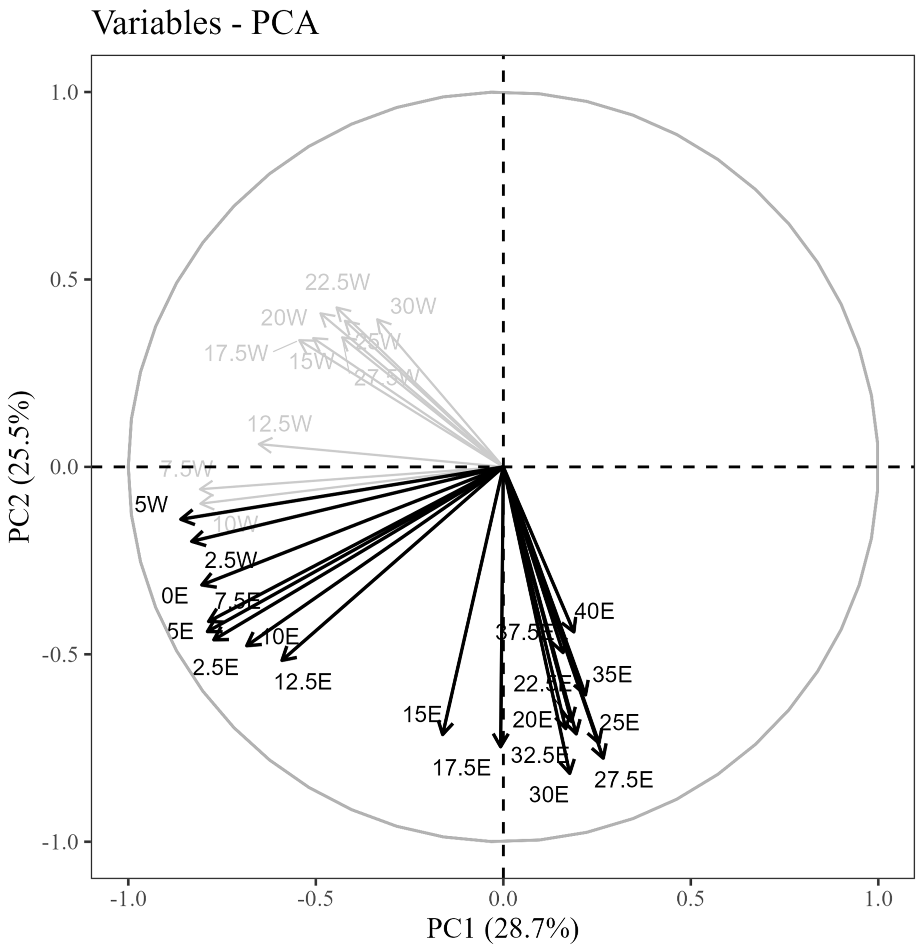

Extended Data Fig. 1 | Principal Component Analysis (PCA) results of summer jet stream latitude (JSL) for the instrumental period (1948–2018 CE). Longitudes that were selected to represent the second mode of July-August EU JSL variability (5° W–40° E; ref. 20) are highlighted in bold. The total explained variance of each PC is shown on the axis title.

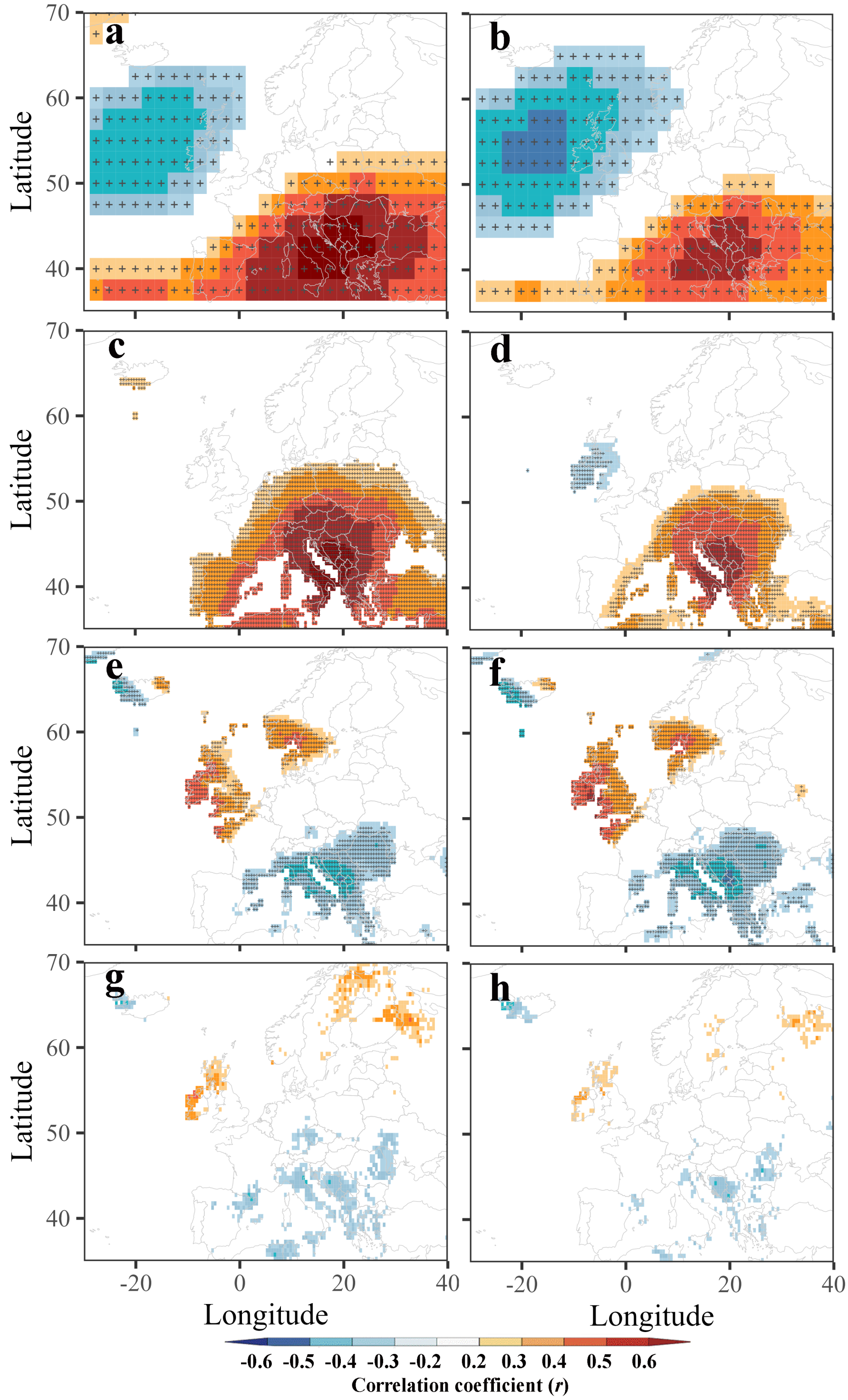

Extended Data Fig. 2 | Spatial Pearson correlations between instrumental summer EU JSL and climate variables in Europe for the period 1948–2018 CE. Panels (a) and (b) show July-August 500 hPa geopotential height from the NCEP/NCAR dataset[67]; (c) and (d) show July-August temperature from the CRU ts4.05 dataset[68]; and (e) and (f) show July-August precipitation from the CRU ts4.05 dataset[68], (g) and (h) show July-August self-calibrating Palmer Drought Severity Index[68]. Panels (a), (c), (e), and (g) show the correlations performed on raw data (both EU JSL and climate variables), whereas (b), (d), (f) and (h) show the correlations performed on linearly detrended instrumental July-August EU JSL and climate datasets. Colored composite maps are shown only where $p \leq 0.1$ and areas with statistically significant values after controlling for the false discovery rate (αFDR ≤ 0.1) are cross-hatched.

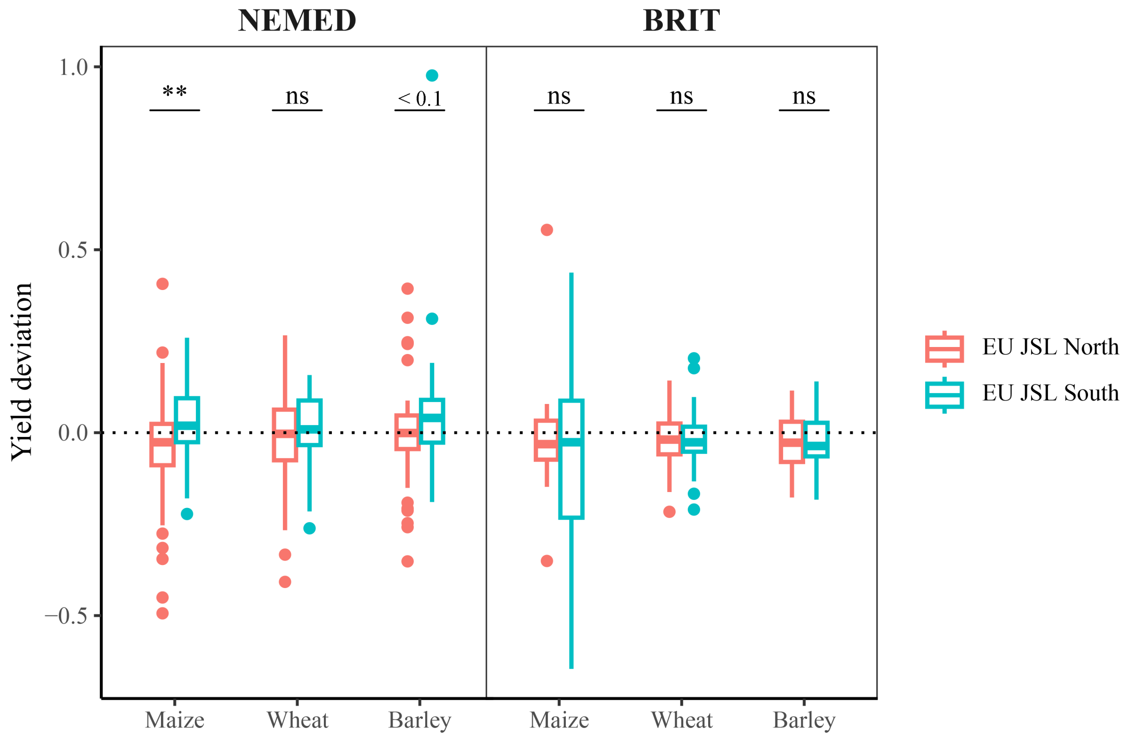

Extended Data Fig. 3 | Influence of summer EU JSL extremes on crop yield during the instrumental period (1961–2018 CE). Boxplots show the distribution of maize, wheat and barley yield during northern (red) versus southern (blue) summer EU JSL extremes in NEMED and BRIT. We determined EU JSL extremes by calculating the D80 (north, $n = 12$ years) and D20 (south, $n = 12$ years) over the period 1961–2018 CE. The lower and upper extremes are indicated by whiskers and dots on each boxplot represent outliers. Significant differences, calculated using a Wilcoxon signed-rank test, are represented by $p < 0.1$ and two ($p \leq 0.01$) asterisks. The "ns" indicates the result is not significant. Crop yield data are derived from the Food and Agricultural Organization (FAO) and were detrended using a 20-year smoothing spline (see Methods).

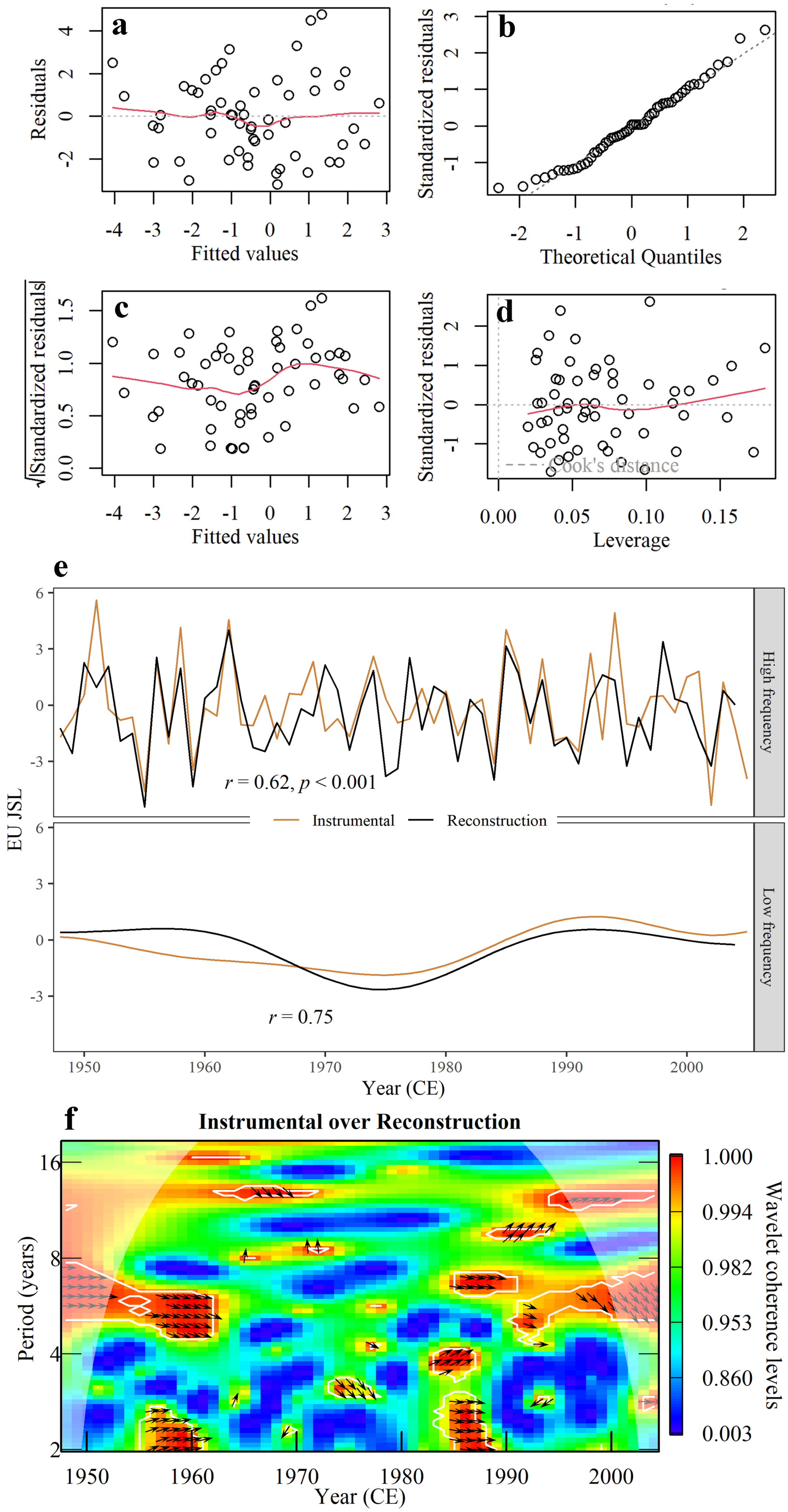

Extended Data Fig. 4 | Variability and distribution of the residuals derived from the multiple linear regression reconstruction model and comparison between reconstructed and instrumental summer EU JSL for the period 1948–2004 CE. (a) Scatter plot between residuals and fitted values in the linear regression, (b) Q-Q plot of the standardized residuals, (c) scatter plot between standardized residuals and fitted values, and (d) scatter plot between standardized residuals and leverage values. The vertical dashed line indicates the Cook's distance in panel (d). The comparison is shown for both high- and low-frequency variability, after applying a 20-year smoothing spline. In panel (e), *r* represents the Pearson correlation coefficient between reconstructed and instrumental EU JSL. For the low-frequency series, the level of significance is not provided since the effective degrees of freedom were not adjusted. Panel (f) shows a complementary cross-wavelet coherency analysis between instrumental and reconstructed summer EU JSL. Instrumental data is derived from the NCEP/NCAR reanalysis product.

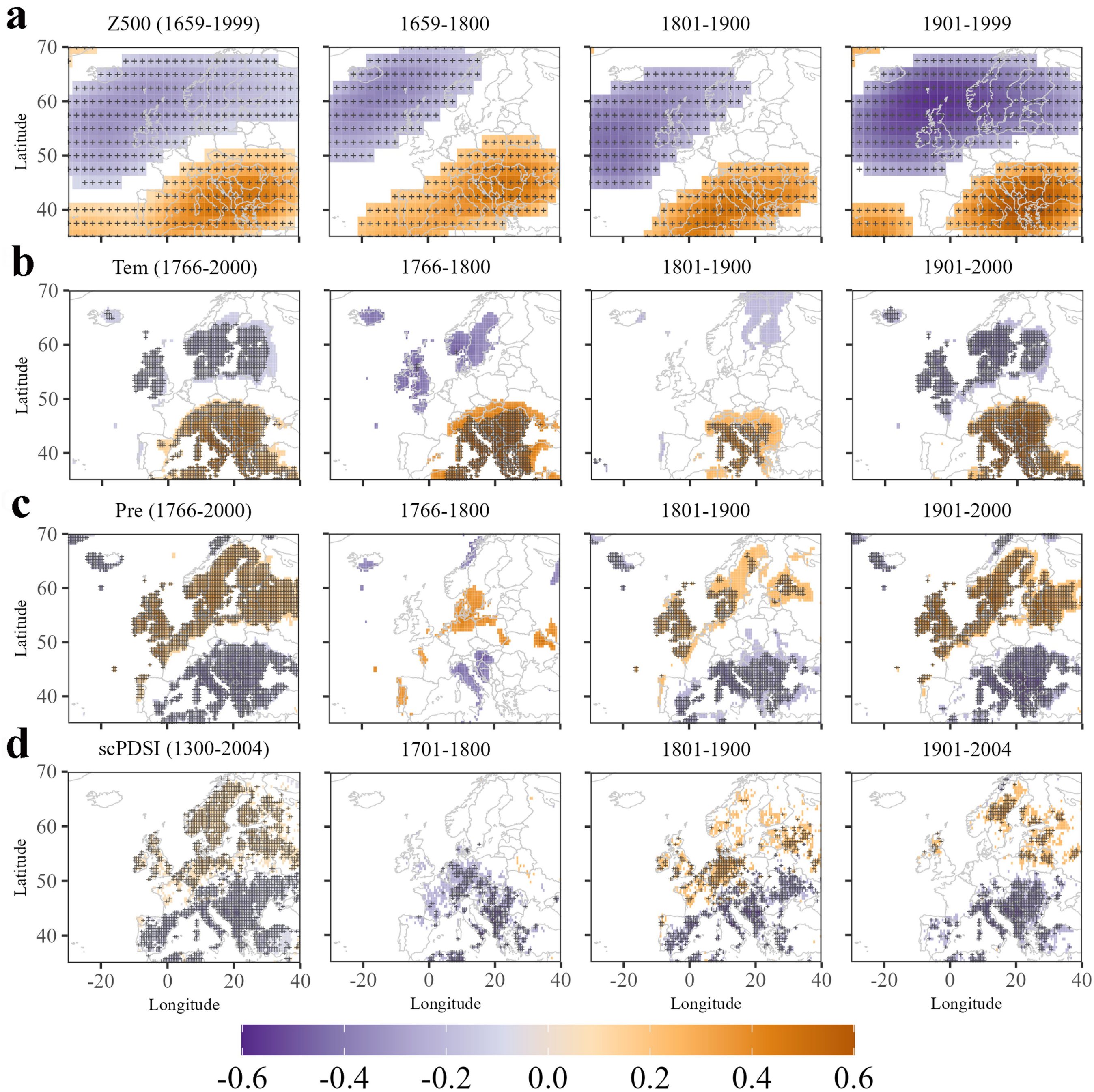

Extended Data Fig. 5 | Spatial correlations between the summer EU JSL reconstruction and gridded July-August climate reconstructions for Europe. (a) July-August 500 hPa geopotential height (Z500)[35] for 1659–1999 CE; (b) July-August temperature[36] for 1766–2000 CE; (c) July-August precipitation[36] for 1766–2000 CE; and (d) June-July-August Old World Drought Atlas (OWDA) self-calibrating Palmer Drought Severity Index (scPDSI)[37] for 1300–2004 CE. Panels in the far-left column show the entire period of overlap between the climate data and the EU JSL reconstruction, followed by the data over three roughly 100-year subperiods: the 18th, 19th, and 20th centuries (from left to right). Colored correlation maps are shown only where $p \leq 0.1$ and areas with statistically significant values after controlling for the false discovery rate (αFDR ≤ 0.1) are cross-hatched.

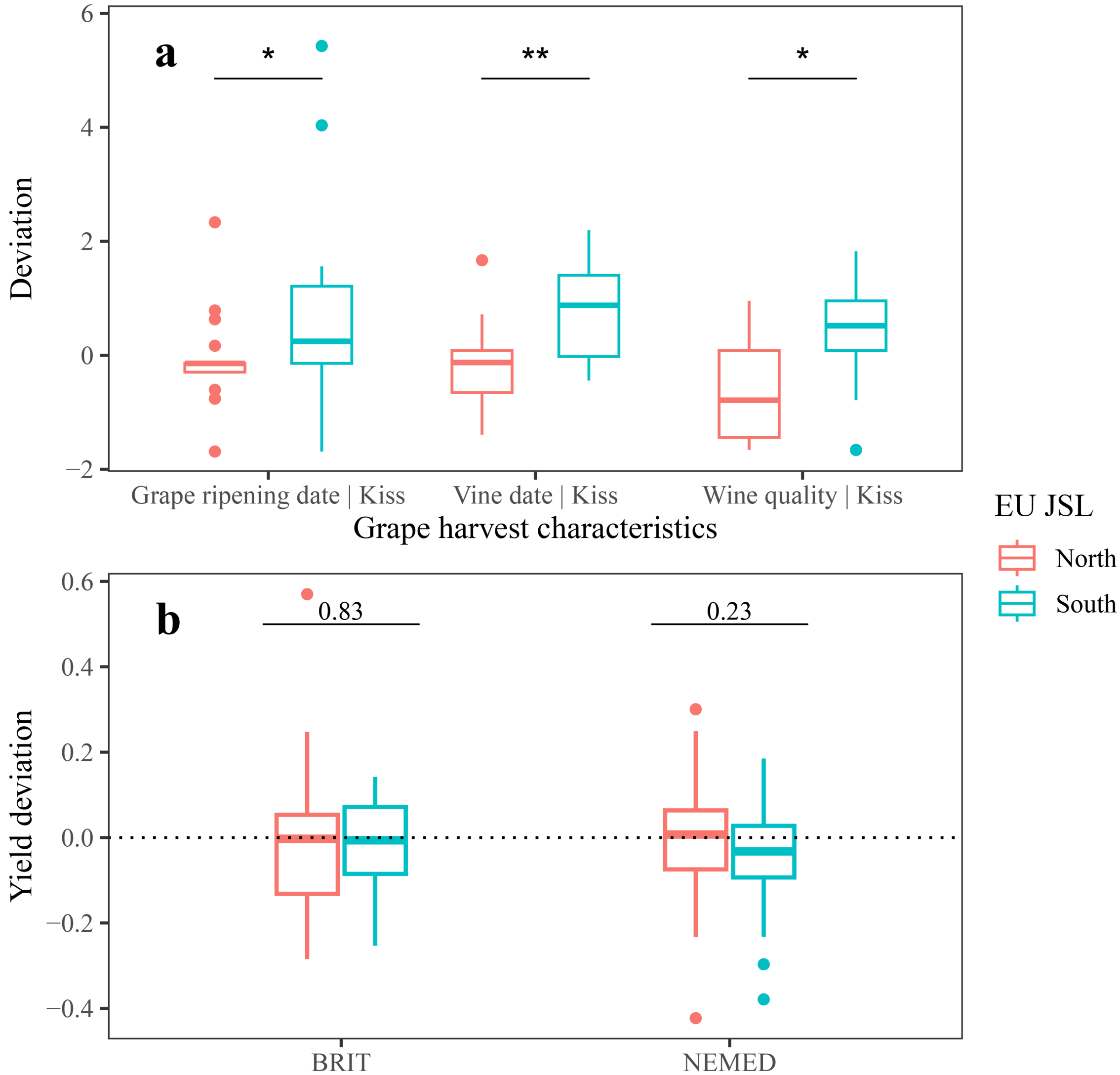

Extended Data Fig. 6 | Influence of summer EU JSL extremes on historical grape phenology and instrumental grape yield. (a) Boxplots showing the distribution of NEMED grape phenology (grape ripening date, vine date, and wine quality) data during historical northern (red) versus southern (blue) summer EU JSL extremes in NEMED region (data for BRIT not available). We determined EU JSL extremes by calculating D90 and D10 values over the period of overlap between grape phenology records and the EU JSL reconstruction. Wine quality deviation values were inversed for visualization purposes. Details of the grape phenology series, such as locations, references, period, and proxies can be found in Extended Data Table 5. (b) Boxplots showing the distribution of instrumental grape yield (1961–2018 CE) during northern (red) versus southern (blue) summer EU JSL extremes in BRIT and NEMED. We determined EU JSL extremes by calculating D80 (north, $n = 12$ years) and D20 (south, $n = 12$ years) values over the instrumental period 1961–2018 CE. Grape yield data are derived from the Food and Agricultural Organization (FAO) and were detrended using a 20-year smoothing spline (see Methods). In panels (a) and (b), we calculated statistical significance in grape phenology and yield distribution using a Wilcoxon signed-rank test. Significant results are represented by one ($p \leq 0.05$) and two ($p \leq 0.01$) asterisks in panel (a) and by p-values in panel (b). The lower and upper extremes are indicated by whiskers, and dots on each boxplot represent outliers.

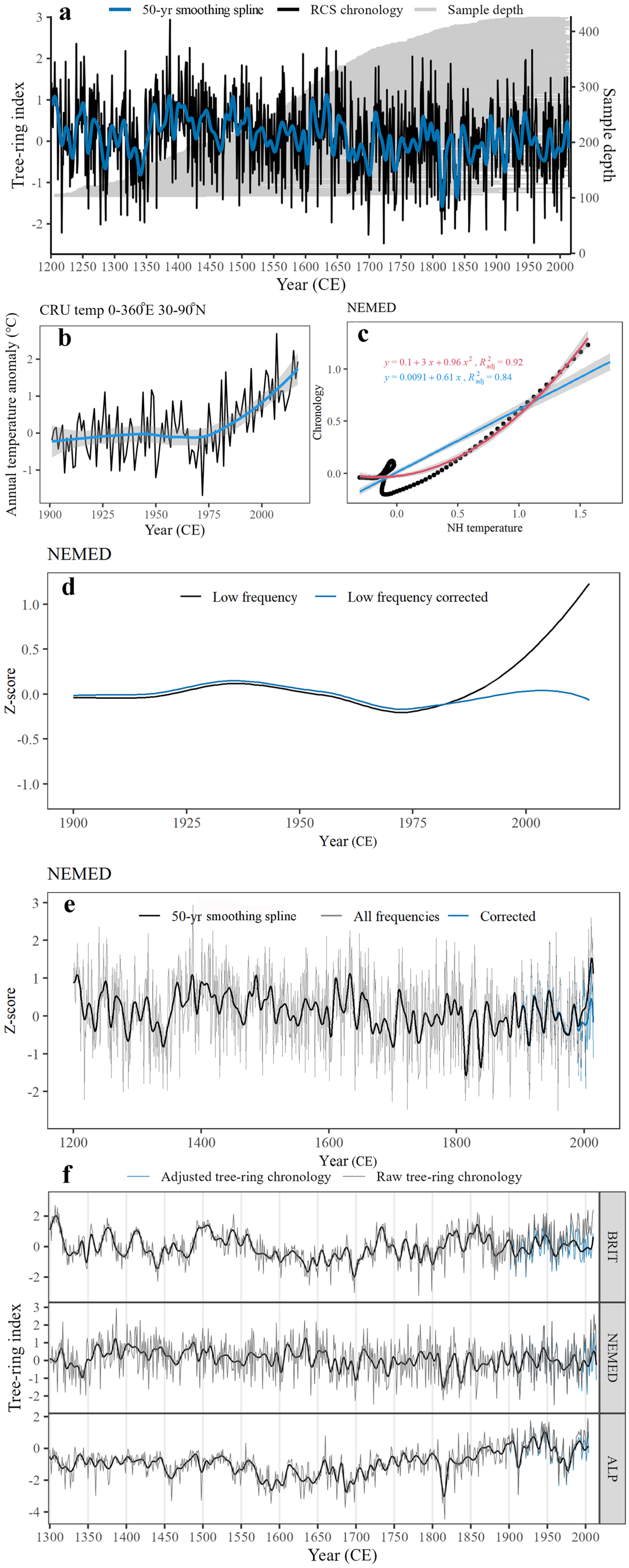

Extended Data Fig. 7 | NEMED chronology, chronology adjustment, and comparison of raw and adjusted chronologies. (a) The NEMED tree-ring maximum latewood density (MXD) chronology and sample depth (horizonal gray lines). The tree-ring chronology was truncated to the year with an expressed population signal (EPS) value above 0.85. The regional curve standardized (RCS) chronology is shown in black, and the low-pass filter (50-year smoothing spline) version of the chronology is shown in blue. Panels (b)-(e) show the scheme of chronology adjustment performed to remove the thermodynamic trend from the tree-ring chronology. The example shown here is for the NEMED chronology. Panel (b) shows interannual (black) and low-frequency (blue) variability of extra-tropical annual Northern Hemisphere (NH) temperature anomalies averaged over 0-360°E and 0-90°N (CRU ts4.05 dataset[68]) and then calculated using a 100-year loess smooth filter. Panel (c) shows the regression lines between the NH low-frequency temperature anomalies and the NEMED tree-ring chronology. Dots represent the raw data; the blue and red curves represent linear and non-linear regressions, respectively. Panel (d) shows the difference in low frequency variability of the original NEMED tree-ring chronology before (black) and after (blue) removing the thermodynamic effect caused by greenhouse gas forcing. In panel (e), low-frequency variability was highlighted by using a 50-year low-pass filter smoothing spline. Panel (f) shows the comparison between raw BRIT, NEMED, and ALP tree-ring chronologies (gray) and the same tree-ring chronologies adjusted after removing the thermodynamic trend (blue). Low-frequency variability of the adjusted chronology is shown in black and was calculated by low-pass filtering the original series using a 50-year smoothing spline. Further information on each chronology can be found in Extended Data Table 2.

Extended Data Table 1 | Years with extreme summer EU JSL position for the instrumental period (1948–2018 CE)

D80 (North)	1951	1958	1962	1985	1986	1988	1992	1994
	2006	2007	2008	2010	2012	2015	2018	
D20 (South)	1955	1957	1959	1964	1966	1970	1971	1972
	1976	1977	1979	1981	1984	2002	2005	

D80 (north) and D20 (south) represent the 80th and 20th percentiles of the instrumental summer EU JSL values, respectively, corresponding to data shown in Fig. 1.

Extended Data Table 2 | Summarized information for the tree-ring chronologies used for the summer EU JSL reconstruction

Region	Code	Period	Species	Tree-ring parameter	Number of series	Reference	*r* with July-August temperature (1901-present)		*r* with EU JSL for the adjusted chronology (1948-present)	
							raw	High-pass filtered#	raw	High-pass filtered#
NEMED	**NEMED**	760-2015	*Pinus heldreichii*	MXD	425	This study; 79-82	0.49**	0.62**	0.47**	0.44**
Alps	**ALP**	755-2004	*Larix decidua*	MXD	180	32	0.55**	0.59**	0.36**	0.19
British	**BRIT**	1300-2010	*Pinus sylvestris*	RW / BI	679	31	0.61**	0.72**	-0.27*	-0.36**

The unfiltered adjusted chronologies were used in the final summer EU JSL reconstruction. MXD represents tree-ring maximum density, RW represents tree-ring width, and BI represents tree-ring blue intensity. #Indicates that a high-pass filter (the difference between the current year and the previous year) was applied. *r* represents Pearson's correlation coefficient. **Represents significance level $p \leq 0.01$ and *represents significance level $p \leq 0.05$ in the table. Data from refs. 31,32,79–82.

Extended Data Table 3 | The stepwise multiple linear regression model selection and calibration and verification statistics for the July-August EU JSL reconstruction

a)

Model: EU JSL ~ NEMED + BRIT + ALP				
Drop	Df	Sum of square	RSS	AIC
None			194.68	78.014
BRIT	1	18.161	221.84	81.097
NEMED	1	31.604	226.28	84.588
ALP	1	49.932	226.61	89.028

Final model: EU JSL ~ NEMED + BRIT + ALP, F = 12.73; Df = 53, R^2_{adj} =38.5%, p < 0.001				
	Estimated coefficient	Std. Error	t value	Pr(>|t|)
(Intercept)	-0.0897	0.2637	-0.340	0.7351
NEMED	0.9165	0.3125	2.933	0.0049
BRIT	-0.8036	0.3614	-2.224	0.0305
ALP	1.1333	0.3074	3.687	< 0.001

b)

Period	**Calibration**		**Verification**		
	R^2_{adj}	**AIC**	R^2_{adj}	**RE**	**CE**
1948-1975	34%	40.03	41%	0.37	0.28
1976-2004	41%	41.27	36%	0.32	0.21
1948-2004	38.5%	78.01			

Table 3a shows the model selection and the coefficients of the final model. Df, Degrees of freedom; RSS, Residual Sum of Squares; AIC, Akaike Information Criterion; and Std. Error, standard error. Table 3b shows the adjusted R^2 (R^2_{adj}), AIC, reduction of error (RE), and coefficient of efficiency (CE) values for the split-period calibration and verification.

Extended Data Table 4 | Years with extreme negative and positive values for each century of the reconstructed summer EU JSL (1300–2004 CE)

1300-1399		1400-1499		1500-1599		1600-1699		1700-1799		1800-1899		1900-2004	
D90	D10	D90	D10	D90	D10	D90	D10	D90	D10	D90	D10	D90	D10
1317	1305	1401	1461	1566	1501	1615	1601	1746	1711	1802	1812	1902	1914
1348	1307	1405	1470		1532	1650	1619	1772	1716	1804	1813	1903	***1955***
1349	1310	1431	1496		1538	1660	1641	1781	1723	1807	1814	1905	***1972***
1382	1320	1436	1498		1539	1662	1646	1782	1730	1877	1815	1909	1975
1386	1327	1438			1540		1652	1784	1735	1879	1816	1917	***1976***
1387	1331	1439			1542		1669	1797	1738	1881	1817	1920	
1394	1353	1441			1557		1675	1799	1740	1885	1819	1921	
	1366	1443			1563		1676		1741	1892	1821	1922	
	1377	1445			1571		1685			1894	1825	1923	
		1482			1578		1686			1895	1833	1927	
		1488			1587		1688				1835	1928	
					1589		1689				1837	1930	
					1592		1690				1838	1932	
							1699				1850	1934	
											1852	1942	
											1857	1943	
											1858	1945	
											1859	1946	
												1950	
												1951	
												1952	
												1956	
												1958	
												1961	
												1962	
												1985	
												1986	
												1993	
												1994	
												1998	
7	9	11	4	1	13	4	14	7	8	10	18	31	5

D10 and D90 represent the 10th and 90th percentiles of the reconstructed EU JSL values, respectively. The bold and italic years are the extreme summer EU JSL years that occur in both the instrumental record (Extended Data Table 1) and the reconstruction. The total number of years in each category is provided in the bottom row.

Extended Data Table 5 | Information on the temperature, precipitation, flood, crop price, grape phenology, wildfire, epidemics, and human mortality data used for the group comparison analyses for BRIT (blue) and NEMED (red) (Figs. 4, 5, and Extended Data Fig. 6)

ID	Parameter	Season	Region	Period	Events	Resolution	Proxy	Ref.
Temperature (Fig 4a)					**Hot / Cold**			
van Engelen	Temperature	Summer	Low Countries	1300-1999	75 / 74	C & categories	Ins & Doc	51
Manley	Temperature	Summer	Central England	1659-2004	35 / 35	C	Ins & Doc	56, 57
Casty	Temperature	July-August	Britain	1766-2000	24 / 24	C	Ins & Doc	36
Kiss	Temperature	May-July	Hungary (Koszeg)	1618-2005	36 / 39	C	Doc	55
Böhm	Temperature	May-July	Hungary (Budapest)	1780-2006	23 / 23	C	Ins & Doc	58
Casty	Temperature	July-August	NEMED	1766-2000	24 / 24	C	Ins & Doc	36
Camuffo	Hot summers	Summer	Italy & Greece	1500-2005	17 / na	D	Ins & Doc	52
Precipitation/floods (Fig 4b)					**Dry / Wet**			
Cole & Marsh	Aridity index	Summer	England & Wales	1766-2003	12 / na	D	Ins & Doc	53
Murphy	Precipitation	August	Ireland	1711-2005	29 / 30	C	Ins & Doc	59
Alexander & Jones	Precipitation	July-August	England & Wales	1711-2016	25 / 25	C	Ins	60
Casty	Precipitation	July-August	Britain	1766-2000	24 / 24	C	Ins & Doc	36
Casty	Precipitation	July-August	NEMED	1766-2000	24 / 24	C	Ins & Doc	36
Pavese	Floods	Summer	Italy	1500-2000	na / 28	D	Doc	54
Grain price (Fig 5a)					**Low / High**			
Clark (wheat)	Wheat price	Annual	England	1300-1800	56 / 53	C	Doc	62
Clark (barley)	Barley price	Annual	England	1300-1800	51 / 49	C	Doc	62
Ljungqvist (wheat)	Wheat price	Annual	BRIT	1300-1800	50 / 50	C	Doc	40
Ljungqvist (wheat)	Wheat price	Annual	Italy	1300-1800	50 / 51	C	Doc	40
Harvest of grapes (Fig 5b; Extended Data Fig 6a)					**Good / Bad**			
Kiss	Wine quality	Summer	Hungary (Koszeg)	1740-1874	16 / 12	C* and categories	Doc	55
Kiss	Church tax – wine date	Summer	Hungary (Koszeg)	1708-1874	17 / 14	C*	Doc	55
Kiss	Vine date	Summer	Hungary (Koszeg)	1618-1874	23 / 27	C*	Doc	55
Kiss	Grape ripening date	summer	Hungary (Koszeg)	1618-1874	16 / 13	C*	Doc	55
Rácz	Poor grape quality	Summer	Carpathian basin	1500-1850	na / 9	D	Doc	61
Rácz	Poor grape quantity	Summer	Carpathian basin	1500-1850	na / 16	D	Doc	61
Wildfire (Fig 5c)								
Christopoulou	Wildfire	Annual	Greece	1845-1940	36†	D	Tree rings	92
Vasileva & Panayotov	Wildfire	Annual	Bulgaria	1450-1940	36†	D	Tree rings	93
Şahan	Wildfire	Annual	Turkey	1652-1940	36†	D	Tree rings	94
Epidemics & mortality (Fig 5c)								
Campbell & Ludlow	Human mortality	Annual	Ireland	1300-1649	49	D	Doc	28
Campbell & Ludlow	Epidemics	Summer	Ireland	1300-1649	40	D	Doc	28
Büntgen	Plague	Annual	NEMED	1346-1910	72	D	Doc	45

The "events" column gives the total number of events in each record and "na" represents not available data; in the "resolution" column, "C" indicates a continuous dataset, C* indicates a continuous dataset with some missing values, whereas "D" indicates a discrete dataset (i.e., a list of discrete event years) and "categories" indicates that the data are classified by their degree of extreme; and in the "proxy" column, "Ins" indicates an instrumental dataset, whereas "Doc" indicates a documentary dataset (i.e., a historical record from documentary data). †36 is the total number of events in all included wildfire studies, which were combined into a single list of events for the analysis. Data from refs. 28,36,40,45,51–62,92–94.